

THE SURVEY FOR IONIZATION IN NEUTRAL GAS GALAXIES: I. DESCRIPTION AND INITIAL RESULTS

GERHARDT R. MEURER¹, D.J. HANISH¹, H.C. FERGUSON², P.M. KNEZEK³, V.A. KILBORN^{4,5}, M.E. PUTMAN⁶, R.C. SMITH⁷, B. KORIBALSKI⁵, M. MEYER², M.S. OEY⁶, E.V. RYAN-WEBER⁸, M.A. ZWAAN⁹, T.M. HECKMAN¹, R.C. KENNICUTT, JR.¹⁰, J.C. LEE¹⁰, R.L. WEBSTER¹¹, J. BLAND-HAWTHORN¹², M.A. DOPITA¹³, K.C. FREEMAN¹³, M.T. DOYLE¹⁴, M.J. DRINKWATER¹⁴, L. STAVELEY-SMITH⁵, AND J. WERK⁶

2006, *ApJS* in press

ABSTRACT

We introduce the Survey for Ionization in Neutral Gas Galaxies (SINGG), a census of star formation in HI-selected galaxies. The survey consists of H α and *R*-band imaging of a sample of 468 galaxies selected from the HI Parkes All Sky Survey (HIPASS). The sample spans three decades in HI mass and is free of many of the biases that affect other star forming galaxy samples. We present the criteria for sample selection, list the entire sample, discuss our observational techniques, and describe the data reduction and calibration methods. This paper focuses on 93 SINGG targets whose observations have been fully reduced and analyzed to date. The majority of these show a single Emission Line Galaxy (ELG). We see multiple ELGs in 13 fields, with up to four ELGs in a single field. All of the targets in this sample are detected in H α indicating that dormant (non-star-forming) galaxies with $M_{\text{HI}} \gtrsim 3 \times 10^7 M_{\odot}$ are very rare. A database of the measured global properties of the ELGs is presented. The ELG sample spans four orders of magnitude in luminosity (H α and *R*-band), and H α surface brightness, nearly three orders of magnitude in *R* surface brightness and nearly two orders of magnitude in H α equivalent width (EW). The surface brightness distribution of our sample is broader than that of the Sloan Digital Sky Survey (SDSS) spectroscopic sample, the EW distribution is broader than prism-selected samples, and the morphologies found include all common types of star forming galaxies (e.g. irregular, spiral, blue compact dwarf, starbursts, merging and colliding systems, and even residual star formation in S0 and Sa spirals). Thus SINGG presents a superior census of star formation in the local universe suitable for further studies ranging from the analysis of HII regions to determination of the local cosmic star formation rate density.

Subject headings: galaxies: ISM – galaxies: evolution – HII regions – stars: formation – surveys

1. INTRODUCTION

Selection biases have had a serious influence in our understanding of the universe. This is especially true with regards to star formation in the local universe. Attempts at a global census of star formation depend critically on the limitations of the methods used.

¹ Department of Physics and Astronomy, Johns Hopkins University, 3400 North Charles Street, Baltimore, MD 21218

² Space Telescope Science Institute, 3700 San Martin Drive, Baltimore, MD 21218

³ WIYN Consortium, Inc., 950 North Cherry Avenue, Tucson, AZ 85726

⁴ Centre for Astrophysics and Supercomputing, Swinburne University of Technology, Mail 31, PO Box 218, Hawthorn, VIC 3122, Australia

⁵ Australia Telescope National Facility, CSIRO, P.O. Box 76, Epping, NSW 1710, Australia

⁶ University of Michigan, Department of Astronomy, 830 Denison Building, Ann Arbor, MI 48109-1042

⁷ Cerro Tololo Inter-American Observatory (CTIO), Casilla 603, La Serena, Chile

⁸ Institute of Astronomy, Madingley Road, Cambridge CB3 0HA, United Kingdom

⁹ European Southern Observatory, Karl-Schwarzschild-Str. 2, 85748 Garching b. München, Germany

¹⁰ Steward Observatory, University of Arizona, Tucson, AZ 85721

¹¹ School of Physics, University of Melbourne, VIC 3010, Australia

¹² Anglo-Australian Observatory, Epping NSW 2121, Australia

¹³ Research School of Astronomy and Astrophysics, Australian National University, Cotter Road, Weston Creek, ACT 2611, Australia

¹⁴ Department of Physics, University of Queensland, Brisbane, QLD 4072, Australia

For example, prism-based emission line samples (e.g. Gallego, et al. 1995; Salzer et al. 2000) are biased toward systems with high equivalent widths; ultraviolet (UV) selected samples (e.g. Treyer, et al. 1998) are biased against very dusty systems; and far-infrared (FIR) selected samples (e.g. Sanders & Mirabel 1996) are biased against low-dust (and perhaps low-metallicity) systems. Broad-band optical surveys have a well-known bias against low surface brightness (LSB) systems (Disney 1976) that are at least as common as normal and “starburst” galaxies (Bothun, Impey, & McGaugh 1997). Conversely, the techniques used to discover LSB systems tend to discard compact and high surface brightness galaxies (Dalcanton et al. 1997), as do surveys that distinguish galaxies from stars by optical structure (Drinkwater et al. 2002). Broad-band surveys from the optical, UV, and infrared also suffer from spectroscopic incompleteness. The missed galaxies are typically faint, may be at low distances, and hence may make major contributions to the faint end of the luminosity function. Large fiber-spectroscopy surveys such as 2dF (Colless et al. 2001) and SDSS (York et al. 2000) are affected by the selection function for placing fibers (e.g. Strauss et al. 2002), large aperture corrections (which are variable even for galaxies of similar morphology; Brinchmann et al. 2004, ; hereafter B04), “fiber collisions” (Blanton et al. 2003), and the requirements for classification as “star forming” (B04). While these effects are mostly small and well studied (e.g. B04), they may still introduce subtle biases in our understanding of

the phenomenology of extra-galactic star formation. Finally, the different tracers of star formation (UV, FIR, $H\alpha$, X-ray and radio emission) result from different physical processes, and often trace different masses of stars. Imprecise knowledge of the physics of these processes and particularly the Initial Mass Function (IMF) may result in systematic errors in the star formation rate (SFR).

A more complete census of star formation in the local universe would be sensitive to all types of star-forming galaxies. Here we report initial results from the Survey for Ionization in Neutral Gas Galaxies (SINGG), which we will show meets this requirement. SINGG surveys HI-selected galaxies in the light of $H\alpha$ and the R -band continuum. $H\alpha$ traces the presence of the highest mass stars ($\mathcal{M}_* \gtrsim 20\mathcal{M}_\odot$) through their ability to ionize the interstellar medium (ISM). For any metallicity, $H\alpha$ (at rest wavelength $\lambda = 6562.82\text{\AA}$) is one of the main emission line coolants in star forming regions and typically the strongest at optical wavelength. The modest typical levels of extinction ($A_{H\alpha} \lesssim 1.5$ mag) found in previous $H\alpha$ surveys (Kennicutt 1983; Gallego et al. 1996; Wegner et al. 2003) suggest that dust absorption corrections are manageable, perhaps even in extremely dusty systems (Meurer & Seibert 2001). The starting point for SINGG is the recently completed HI Parkes All-Sky Survey (HiPASS; Meyer et al. 2004) the largest survey to select galaxies entirely by their HI 21-cm emission. Helmboldt et al. (2004) have also obtained R and $H\alpha$ observations (as well as B band data) of a sample of HiPASS galaxies similar in number to those whose images we present here. Since their goals were more oriented toward studying low surface-brightness galaxies, their sample selection was less comprehensive than ours. Our sample is more inclusive, for instance having no angle of inclination selection, and our observations generally have higher quality and are deeper. Because interstellar hydrogen is the essential fuel for star formation, HiPASS is an ideal sample to use in star formation surveys. HI redshifts are available for all sources thus allowing a consistent measurement of distance. Furthermore, because it is a radio-selected survey, it is not directly biased by optical properties such as luminosity, surface brightness, or Hubble type. Instead, the distribution of these properties that we find will be determined by their dependence on the HI selection criteria we adopt.

This paper describes SINGG and presents initial results for a subsample of targets. Section 2 describes the sample selection process and lists the full SINGG sample. The rest of the paper concentrates on the first subsample of SINGG data that has been fully reduced and analyzed. It consists of 93 SINGG targets observed over four observing runs. Since we are releasing these data, with the publication of this paper, we refer to this data set as SINGG Release 1, or SR1. Section 3 describes the SR1 data and their reduction and analysis. A database of the measured properties is presented in Section 4 which includes a detailed discussion of data quality and errors. Science results are discussed in Sec. 5. Chief among them is that all targets in SR1 are detected in $H\alpha$. These cover a wide range in $H\alpha$ luminosity, surface brightness and equivalent width, verifying that an HI-selected sample is well suited for star formation surveys. We discuss the implications of this result and how the relationship be-

tween star formation and HI may arise. The paper is summarized in Sec. 6.

2. SAMPLE SELECTION

The full list of SINGG targets was selected from HiPASS source catalogs. HiPASS used the 64-m Parkes Radio Telescope with a multibeam receiver (Staveley-Smith et al. 1996) to map the entire southern sky for neutral hydrogen emission from -1280 to $12,700$ km s^{-1} in heliocentric radial velocity (V_h). The original survey, and the source catalogs used for SINGG, extend from -90° to $+2^\circ$ in declination. The northern extension of the survey, $+2^\circ$ to $+25^\circ$ in declination, has recently been cataloged (Wong et al. 2005a). Processing of the HiPASS data resulted in cubes $8^\circ \times 8^\circ$ in size with a velocity resolution of 18.0 km s^{-1} , a spatial resolution of $\sim 15'$, and a 3σ limiting flux of 40 mJy beam^{-1} . (Zwaan et al. 2004) determined the completeness of the survey using a fake source analysis: fake sources were inserted into the HiPASS data cubes and the HiPASS source finder was used to determine whether the source was detected. The fake sources had a wide range of peak fluxes, integrated fluxes, random velocities, and a variety of velocity profile shapes (Gaussian, double-horn, and flat-top) and FWHM velocity widths ranging from 20 to 650 km s^{-1} . Integrated over all profile shapes and widths, the 95% completeness level for integrated flux is 7.4 Jy km s^{-1} (Zwaan et al. 2004) and corresponds to an HI mass limit of $\mathcal{M}_{\text{HI}} \approx 1.7 \times 10^6 \mathcal{M}_\odot D^2$, where D is the distance in Mpc. The details of the observing and reduction methods of HiPASS are outlined in Barnes et al. (2001). In this section we describe how the full SINGG sample was chosen from the HiPASS catalogs, while the rest of the paper focuses on the targets comprising SR1.

2.1. Sample size

The primary goal of SINGG is to uniformly survey the star formation properties of HI-selected galaxies across the entire HI mass function sampled by HiPASS in a way that is blind to previously known optical properties of the sources. An essential aspect of the project is its ability to measure not only mean star formation quantities, but also the distribution about the mean among galaxies of different HI mass (\mathcal{M}_{HI}), Hubble type, surface brightness, and environment. Our goal is to image 180 targets per decade of \mathcal{M}_{HI} . The available sources found by HiPASS allow this goal to be obtained over the mass range $\log(\mathcal{M}_{\text{HI}}/\mathcal{M}_\odot) \approx 8.0$ to 10.6 . A sample this size allows the width in the $H\alpha$ emissivity ($F_{H\alpha}/F_{\text{HI}}$, where $F_{H\alpha}$ and F_{HI} are the integrated $H\alpha$ and HI fluxes) distribution to be measured to statistical accuracy better than 10% per decade of \mathcal{M}_{HI} and allows sensitive tests for non-Gaussian distributions. This is important for testing models such as the stochastic self-propagating star formation scenario of Gerola, Seiden, & Schulman (1980) which predicts a wider range of star-formation properties with decreasing galaxy mass. A large sample also makes the selection of rare systems more likely, including extreme starburst and dormant systems.

2.2. Source catalogs

Our final sample was selected primarily from two catalogs known as HICAT and BGC. (1) HICAT, the full

TABLE 1
CORRELATION OF SINGG SAMPLE AND HIPASS CATALOGS

Catalog	Targets in common		HI parameters source		Reference
	SINGG all	SR1	SINGG all	SR1	
HICAT	450	89	449	89	Meyer et al. (2004)
BGC	269	83	4	3	Koribalski et al. (2004)
SCCC	19	7	0	0	Kilborn et al. (2002)
AVCC	10	6	0	0	Putman et al. (2002)
Additional	15	1	15	1	This study
Total	–	–	468	93	

HiPASS catalog (Meyer et al. 2004) selects candidate sources from the HiPASS cubes using two different automated techniques: a peak flux density threshold algorithm, and a technique of convolving the spectral data with top-hat filters of various scales. Extensive automated and eye quality checks were used to verify candidates. HICAT only includes targets with Galactic standard of rest velocity, $V_{\text{GSR}} > 300 \text{ km s}^{-1}$, in order to minimize the contribution of high velocity clouds (HVCs), and was created totally blind to the optical properties of the targets. The completeness and reliability of this catalog are well understood (Zwaan et al. 2004), hence it was the primary source for our sample selection and all HI parameters. (2) The HiPASS Bright Galaxy Catalog (BGC) contains the 1000 HiPASS targets with the brightest peak flux density (Koribalski et al. 2004). The BGC uses the same input data cubes as HICAT; however, it catalogs sources to lower radial velocities. Special attention was paid to insure that all known nearby galaxies were considered for inclusion, irrespective of velocity and confusion with Galactic HI. Care was taken to split the HI flux from contaminating sources, especially Galactic HI.

In Table 1 we break down our sample by membership in various HiPASS catalogs. While HICAT and BGC are our primary source catalogs, due to the concurrent development of the SINGG and HiPASS projects, preliminary versions of these catalogs had to be used in our selection. Likewise, related HiPASS catalogs such as the South Celestial Cap Catalog (SCCC) of Kilborn et al. (2002) and the Anomalous Velocity Cloud Catalog (AVCC) of Putman et al. (2002) were used in our earliest selections.

A comparison of our final selection and the published HICAT and BGC reveals 14 sources not in the published version of the catalogs. These made it into our sample for one of three reasons: (1) those located just to the north of the final HICAT declination cut, $\delta = 2^\circ$ made it into the version of HICAT used in our selection but were eliminated from the published version; (2) similarly, some sources near the detection limit of the cubes did not make it into the final HICAT; finally (3) sources from earlier selections that were already observed in our survey were “grandfathered” into the SINGG sample. We carefully examined the HiPASS data for all targets in our sample that were neither in the final HICAT nor BGC, in order to check their reality. Real sources are those whose angular size is equal to the beam size, or up to a few times larger, have peak fluxes clearly above the noise level, and do not correspond to baseline ripples, as determined by cuts at constant velocity right ascension and declination through the data cubes. Sources that did not meet these

criteria were rejected from our final sample. The HI properties of the 14 detections neither in HICAT nor BGC were measured using the standard procedure adopted in BGC. As was done for BGC creation, special care was taken to split sources that appear double or which are barely resolved spatially at the $15'$ resolution of the HiPASS data. The HI properties of these sources with new measurements are given in Table 2. In addition there is one source in this table, HiPASS J1444+01, which is also in HICAT but very close spatially and in velocity to one of the new measurements, HiPASS J1445+01. We adopt our new measurements as an improved splitting of the HI flux.

2.3. Selection criteria

We selected “candidate” targets from the source catalogs using the following criteria: (a) peak flux density, $S_p \geq 0.05 \text{ Jy}$; (b) Galactic latitude, $|b| > 30^\circ$; (c) projected distance from the center of the LMC, $d_{\text{LMC}} > 10^\circ$; (d) projected distance from the center of the SMC, $d_{\text{SMC}} > 5^\circ$; (e) Galactic standard of rest velocity, $V_{\text{GSR}} > 200 \text{ km s}^{-1}$; and (f) V_h not within 100 km s^{-1} of the following “bad” velocities: 586, 1929, 2617, 4279, 4444, 5891, 10155 and 10961 km s^{-1} . Condition a insures that only sources with adequate S/N are used. It requires that the *peak* signal-to-noise ratio $S/N > 3.8$ in the HI spectra. As noted in Sec. 2.2, our selection was from preliminary versions of HICAT and BGC; hence not all the sources in our final sample meet this criterion when using the published catalogs (4% of our sample have $S_p < 0.05 \text{ Jy}$). Conditions b-d minimize foreground dust and field star contamination from the Galaxy and Magellanic Clouds. Condition e minimizes contamination from HVCs. Condition f was included to avoid radio frequency interference features and Galactic recombination lines found in some preliminary HiPASS catalogs. It should be noted that the final HICAT and BGC have been effectively cleansed of these sources of interference (Meyer et al. 2004; Koribalski et al. 2004).

Our sample was selected from the candidates defined above based on HI mass, \mathcal{M}_{HI} , and distance D . The mass is derived from the integrated HI flux $F_{\text{HI}} = \int f_\nu d\nu$ in Jy km s^{-1} and D in Mpc using the formula

$$\mathcal{M}_{\text{HI}} = 2.36 \times 10^5 \mathcal{M}_\odot D^2 F_{\text{HI}} \quad (1)$$

(Roberts 1962). The value of D is derived from V_h corrected for a model of the local Hubble flow. Specifically, we employ the multi-pole attractor model of the H_0 key project as discussed by Mould et al. (2000) and adopt $H_0 = 70 \text{ km s}^{-1} \text{ Mpc}^{-1}$. This is the only distance estimate used during sample selection. Final distances are discussed in Sec. 2.4.

TABLE 2
ADDITIONAL HI MEASUREMENTS FROM HIPASS DATA

HiPASS+ (1)	RA (2)	Dec. (3)	S_p (4)	F_{HI} (5)	V_h (6)	W_{50} (7)	W_{20} (8)
J0249+02	02 49 06	+02 08 11	1.033	56.4	1104	56	73
J0400−52	04 00 33	−52 41 27	0.053	7.5	10566	298	349
J0412+02	04 12 47	+02 21 20	0.069	13.6	5017	393	424
J1145+02	11 45 03	+02 09 57	0.163	5.6	1010	30	51
J1208+02	12 08 00	+02 49 30	0.435	66.6	1322	200	223
J1210+02	12 10 57	+02 01 49	0.127	10.0	1337	80	97
J1211+02	12 11 40	+02 55 30	0.085	5.2	1295	88	108
J1234+02B	12 34 20	+02 39 47	0.469	103.1	1737	355	381
J1234+02A	12 34 29	+02 12 41	0.344	77.0	1805	326	348
J1326+02A	13 26 20	+02 06 24	0.119	17.1	1090	152	177
J1326+02B	13 26 20	+02 27 52	0.049	1.9	1026	38	54
J1328+02	13 28 12	+02 19 49	0.063	3.0	1023	50	66
J1444+01	14 44 28	+01 42 45	0.146	33.0	1569	323	351
J1445+01	14 45 00	+01 56 11	0.098	28.9	1727	625	645
J2000−47	20 00 58	−47 04 11	0.067	16.2	6551	310	657

NOTE. — Column descriptions [units]: (1) Source name. (2) and (3) Right ascension and declination [J2000]. (4) Peak flux density of HiPASS 21cm spectrum [Jy]. (5) Integrated HI flux [Jy km s^{−1}]. (6) Systemic heliocentric velocity of HI measured as the mid-point at the 50% of S_p level [km s^{−1}]. (7) Width of HI profile at 50% of S_p [km s^{−1}]. (8) Width of HI profile at 20% of S_p [km s^{−1}].

When selecting sources, we divided the candidates into $\log(\mathcal{M}_{\text{HI}})$ bins and preferentially selected the nearest objects in each bin to populate our selection. This preference allows better morphological information and a more accurate determination of the HII region luminosity function and also minimizes confusion in the HI detections. The distance preference was not rigorously enforced in order to allow sources we had already observed to be grandfathered into the sample. A total of 64 galaxies in our final selection would not meet a strict distance preference selection.

Our final adopted \mathcal{M}_{HI} selection bin width is 0.2 dex. We found that using a bin size of 0.4 dex, or greater, results in noticeable biasing within each bin, in the sense that at the high-mass end, the galaxies selected tend to be in the lower half of the bin in terms of $\log(\mathcal{M}_{\text{HI}})$ and D . The sense of the bias is reversed for the low-mass bins. The bias is negligible for a bin width of 0.2 dex. Using a smaller selection bin size would be meaningless in the face of the D and flux errors. For $\log(\mathcal{M}_{\text{HI}}/\mathcal{M}_{\odot}) < 8.0$ and $\log(\mathcal{M}_{\text{HI}}/\mathcal{M}_{\odot}) > 10.6$ there are less than 180 candidates per decade of \mathcal{M}_{HI} . At the low-mass end the sample is limited to the small volume over which such a low-mass can be detected, while at the high-mass end the number of sources is limited by their rarity. Effectively, we are selecting all HiPASS targets that meet our candidate constraints in both of these mass ranges.

2.4. Final HI parameters

The full SINGG sample is listed in Table 3. Figure 1 compares the $\log(\mathcal{M}_{\text{HI}})$ histogram of the full SINGG sample with the parent distribution of candidate targets. Figure 2 shows the V_h histogram of the full SINGG sample. To keep the measurements homogeneous, we took measurements from HICAT where possible, and used measurements from BGC, or Table 2 for the sources neither in HICAT nor BGC.

Due to small changes in the HI parameters from the

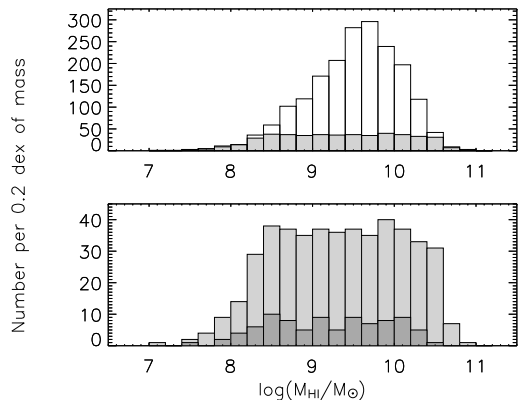


FIG. 1.— HI mass histograms. The top panel shows the candidates from HICAT as the plain histogram, and the SINGG selection as the shaded histogram. The bottom panel zooms in on the y scale showing the total SINGG sample selection in light shading and the SR1 targets as the dark shaded histogram.

preliminary catalogs used in the sample selection, and the final HICAT and BGC catalogs used for the adopted measurements, the $\log(\mathcal{M}_{\text{HI}})$ histogram of the sample shown in Fig. 1 is not exactly “flat” over the mass range of $\log(\mathcal{M}_{\text{HI}}/\mathcal{M}_{\odot}) = 8$ to 10.6.

Hubble flow distances are intrinsically uncertain due to random motions about the flow, the “peculiar velocity dispersion”. Estimates of this range from about 100 to 400 km s^{−1} (e.g., Lynden-Bell et al. 1988; Strauss, Cen, & Ostriker 1993; Willick et al. 1997; Willick & Strauss 1998; Tonry et al. 2000) depending on galaxy type and environment. Within 7 Mpc the value may be as low as ~ 70 km s^{−1} (Macció, Governato & Horrelou 2005). If we adopt 125 km s^{−1} for the peculiar velocity dispersion of field spirals (Willick et al. 1997; Willick & Strauss 1998), then at the median Hubble flow distance of the full SINGG

TABLE 3
FINAL SINGG SAMPLE

HIPASS+ (1)	V_h (2)	W_{50} (3)	D (4)	$\log(\mathcal{M}_{\text{HI}})$ (5)	$E(B-V)$ (6)	SR1 (7)	Catalogs (8)
J0005–28	737	52	10.7	8.27	0.017	Y	HB
J0008–34	221	30	3.3	7.17	0.012	N	B
J0008–59	7786	353	112.1	10.68	0.012	N	H
J0014–23	468	171	7.0	9.40	0.021	N	HBA
J0019–22	670	121	9.8	8.55	0.019	Y	HB
J0030–33	1580	457	22.3	10.23	0.018	N	HB
J0031–22	539	47	7.9	8.01	0.018	Y	HB
J0031–10	3573	286	50.1	10.29	0.032	N	HB
J0034–08	1652	220	23.4	9.95	0.044	N	HB

NOTE. — *Sample portion of table.*

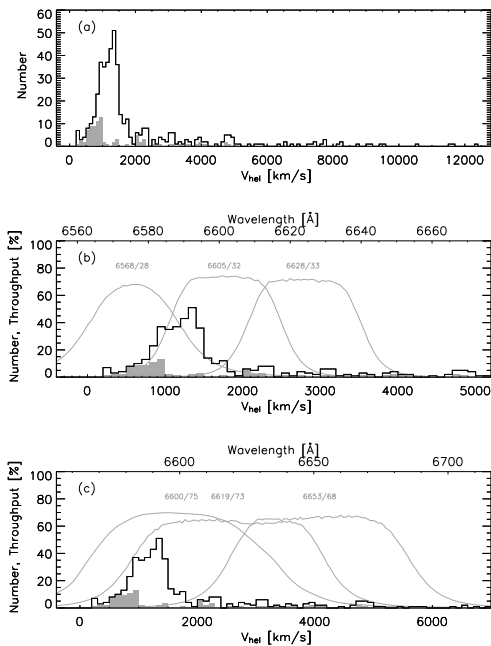


FIG. 2.— Heliocentric radial velocity histogram for the SINGG sample. All panels show the full SINGG sample as an open histogram, and the SR1 targets as the shaded histogram. Panel (a) shows the full velocity range of the sample. Panel (b) over-plots, in gray, SINGG and MCELS $H\alpha$ filter throughput curves combined with the CCD QE curve on an expanded velocity scale histogram. Panel (c) likewise over-plots the throughput curves for the KPNO filters used in run 02.

sample, 18.5 Mpc, we have an intrinsic distance uncertainty of 10% leading to a 20% luminosity error. These uncertainties are much more significant for the nearest sources in our sample. We used the Catalog of Neighboring Galaxies (Karachentsev et al. 2004) to improve the distances to the nearest galaxies in our sample. We adopt 15 matches between this catalog and our sample including only galaxies with D based on Cepheid variables (2 cases), red giant branch measurements (12 cases) or group membership (1 case). We did not include distances from this catalog based on the brightest stars or the Hubble flow out of concern for the accuracy of the distances. Likewise, we did not use Tully-Fisher relationship distances since this relationship is usually calibrated with spiral galaxies and is less reliable for low luminosity, low velocity width galaxies (McGaugh et al. 2000) which

TABLE 4
CTIO 1.5 M OBSERVING RUNS IN SR1

Run #	Dates	Filters used	Targets observed
01	23-27 Oct, 2000	6568/28, 6850/95, R	20
02	26-30 Dec, 2000	6600/75, 6619/73, 6653/68, R	25
03	13-15 Feb, 2001	6568/28, R	21
06	12-15 Sep, 2001	6568/28, 6605/32, 6628/33, R	27

dominate our sample in the local volume. The HiPASS targets with improved distances are marked in Table 3 with an asterisk (*).

3. DATA AND ANALYSIS

3.1. Observations

The SINGG observations were primarily obtained with the Cerro Tololo Inter-American Observatory (CTIO) 1.5 m telescope as part of the NOAO Surveys program. Additional observations were obtained with the CTIO Schmidt and 0.9 m telescopes and the Australian National University 2.3 m at Siding Spring Observatory. In this paper, we present observations from four CTIO 1.5 m observing runs consisting of images obtained with the 2048×2048 CFCCD. The plate scale of $0.43'' \text{ pixel}^{-1}$ produces a $14.7'$ field of view, well matched to the Parkes 64 m beam width. Table 4 presents a brief synopsis of these runs, whose data comprise SINGG Release 1 (SR1). The \mathcal{M}_{HI} and V_h distributions of the SR1 targets are compared with the full SINGG sample in Fig. 1 and 2, respectively.

The images were obtained through narrow-band (NB) filters chosen to encompass redshifted $H\alpha$, as well as R -band images used for continuum subtraction. For three sources (HIPASS J0403–01, HIPASS J0459–26, and HIPASS J0507–37), continuum observations were obtained through a narrower filter, 6850/95, which excludes $H\alpha$ from its bandpass. This was done to test the filter’s use in continuum subtraction or to avoid saturation. Table 5 list the properties of the filters used in this study. The bandpasses of the NB filters are plotted in Fig. 2. These filters include the primary filters used in this survey, which are $\sim 30\text{\AA}$ wide and used to observe galaxies with $V_h < 3300 \text{ km s}^{-1}$, as well as four broader filters used to extend the velocity coverage of the survey. The lowest velocity filter used here, 6568/28, was borrowed from the Magellanic Clouds Emission Line Survey

(MCELS; Smith et al. 1998). We purchased additional filters, two of which are used in this study 6605/32, and 6628/33. The remaining filters are from NOAO’s collection at CTIO or KPNO. The SINGG and MCELS filters were scanned with beams using a range of incident angles at NOAO’s Tucson facility. The scans were used to synthesize the bandpass through an $f/7.5$ beam. Filter properties are listed in Table 5.

To perform the observations, the telescope was positioned to place the HiPASS position near the center of the CCD for each target observed. Typically, the observations consisted of three 120 s duration R exposures (or 3×200 s with 6850/95) and three NB exposures of 600 s duration. The observations were obtained at three pointing centers dithered by $0.5'$ to $2'$ to facilitate cosmic ray and bad column removal.

3.2. Basic processing

Basic processing of the images was performed with *IRAF*¹⁵ using the *QUADPROC* package and consisted of (1) fitting and subtraction of the bias level as recorded in the overscan section of the images, (2) subtraction of a bias structure frame typically derived from the average of 15 to 100 zero frames (CCD readouts of zero duration), and (3) flat-field division. Flat-field frames were obtained employing an illuminated white spot on the dome as well as during evening and/or morning twilight. The final flat-field frames combine the high spatial frequency structure from the dome flats with the low spatial frequency structure from the sky flats. They were made by (a) combining the dome flats with cosmic ray rejection; (b) normalizing the result to unity over the central portion of the frame; (c) dividing the sky flats with the normalized dome flat; (d) combining the sky flats, taking care to scale and weight the images to compensate for the different exposure levels; (e) box median filtering the result with a box size of 25 to 51 pixels on a side; (f) normalizing the result; and (g) dividing the result into the normalized dome flat produced in step b.

3.3. Red leak correction

Examination of the images showed that flat-fielding worked correctly for most filters; the sky was flat to better than 1%. However, this was not the case for many of the 6568/28 images. Figure 3 shows the nature of the problem: an oblong diffuse emission “hump” peaking on one side of the frame covering $\sim 25\%$ of the field of view, with an intensity up to $\sim 30 - 40\%$ of the sky background. This feature was intermittent in nature. For the data presented here, the hump was only seen in runs 03 and 06. Run 01 used 6568/28 exclusively as the NB filter but is not affected, while run 02 did not employ this filter. Most, but not all, later observing runs that used this filter were affected by this feature. Within a run, this feature was variable in amplitude, although its shape remained stable. Examination of individual dithered frames reveal that the count rate of stars is not affected as they are dithered off and on the hump region. We attribute this artifact to a red leak in the filter

coating, allowing the filter to transmit the bright OH sky lines at $\lambda > 6800\text{\AA}$. The variability in amplitude would then result from the variability of these lines.

To remove the hump, we created a set of normalized correction images. For each affected run, at least 15 object images using the 6568/28 filter were selected, preferably those where the target galaxy was small, and did not extend into the hump region. Each image was masked for bad pixels, smoothed with a 7×7 box median to remove cosmic rays, sky subtracted and then normalized to have a peak in the hump of 1.0. The images for each observing run were then combined (with rejection) to remove stars, galaxies, and other sources, and the resulting image was again median-smoothed (9×9) to remove any remaining artifacts of the combine process. Each affected image was manually adjusted by subtracting a scaled version of this correction image. Typically, the scaling was determined from the intensities of ~ 2500 pixels surrounding the brightest point of the feature, after a first pass background sky subtraction.

3.4. Flux calibration

We used observations of spectrophotometric standards (Hamuy et al. 1992 1994; Massey et al. 1988; Oke 1990) to flux calibrate the data. The standards were typically obtained in three sets (at the beginning, middle and end of each night) of two standards each. We calibrated magnitudes in the ABmag system (See Fukugita et al. 1996, for a discussion of the ABmag system and its motivation), and $H\alpha$ line fluxes in terms of $\text{erg cm}^{-2} \text{s}^{-1}$ using synthetic photometry techniques as detailed in Appendix A.

3.5. Combining images

In order to align the images and subtract the continuum, we make use of software kindly provided by the High- z supernova group (Schmidt et al. 1998) and modified by our team. As illustrated in Fig. 4, this provides superior final continuum subtracted images when compared to those of more “traditional” processing, which would typically consist of linearly interpolating all images to a common origin, combining the images in each filter, and performing a straight scaled R -band image subtraction from the NB image. Our processing is somewhat more sophisticated, as follows.

Sources in the individual frames are cataloged using the Source Extractor (SE) software package (Bertin & Arnouts 1996). The catalogs include source positions, fluxes, and structural parameters. They are used to align all the frames of each target to a common reference image - typically the R -band frame in the center of the dither pattern. This is done by matching the catalogs to derive a linear transformation in each axis (allowing offset, stretch, rotation and skew). On the order of 100 matches per frame are typically found. Registration is done with a 7×7 sinc interpolation kernel to preserve spatial resolution and the noise characteristics of the frames. The images in each filter are then combined in IDL using a modified version of *CR_REJECT* found in the *ASTROLIB* package. Our modifications remove sky differences between frames and use the matched catalogs to determine the multiplicative scaling between frames to bring them to the same flux scale. For each filter, the reference image for flux scaling is the one whose

¹⁵ *IRAF* is the Image Reduction and Analysis Facility, and is distributed by the National Optical Astronomy Observatories, which are operated by the Association of Universities for Research in Astronomy, Inc., under cooperative agreement with the National Science Foundation.

TABLE 5
FILTER PROPERTIES

Filter (F) (1)	Owner (2)	$\max(T_F)$ (3)	$\lambda_{p,F}$ (4)	$\lambda_{m,F}$ (5)	$W_{50,F}$ (6)	$W_{E,F}$ (7)	ϵ_C/C (8)
6568/28	MCELS	0.68	6575.5	6575.5	28.1	21.2	0.042
6605/32	SINGG	0.74	6601.5	6601.5	32.5	25.0	0.024
6628/33	SINGG	0.72	6623.7	6623.7	33.1	24.6	0.024
6600/75	CTIO	0.70	6600.7	6600.8	69.4	49.4	0.043
6619/73	KPNO	0.65	6618.0	6618.0	73.7	49.1	0.031
6653/68	KPNO	0.68	6652.2	6652.3	68.2	47.5	0.043
6709/71	KPNO	0.68	6708.4	6708.4	70.6	48.8	0.043
6850/95	MCELS	0.72	6858.9	6859.0	94.6	70.1	—
R	CTIO	0.67	6507.5	6532.4	1453.4	977.0	—

NOTE. — Column descriptions [units]: (1) Filter name. (2) Owner of filter. (3) Peak throughput [dimensionless]. (4) Pivot wavelength [\AA]. (5) Response weighted mean wavelength [\AA]. (6) Transmission profile width at 50% of the peak transmission [\AA]. (7) Response weighted equivalent width of the filter [\AA]. (8) The adopted ratio for the error due to continuum subtraction divided by the continuum flux. Definitions for $\lambda_{p,F}$, $\lambda_{m,F}$, and $W_{E,F}$ (columns 4,5 and 7) can be found in appendix A.

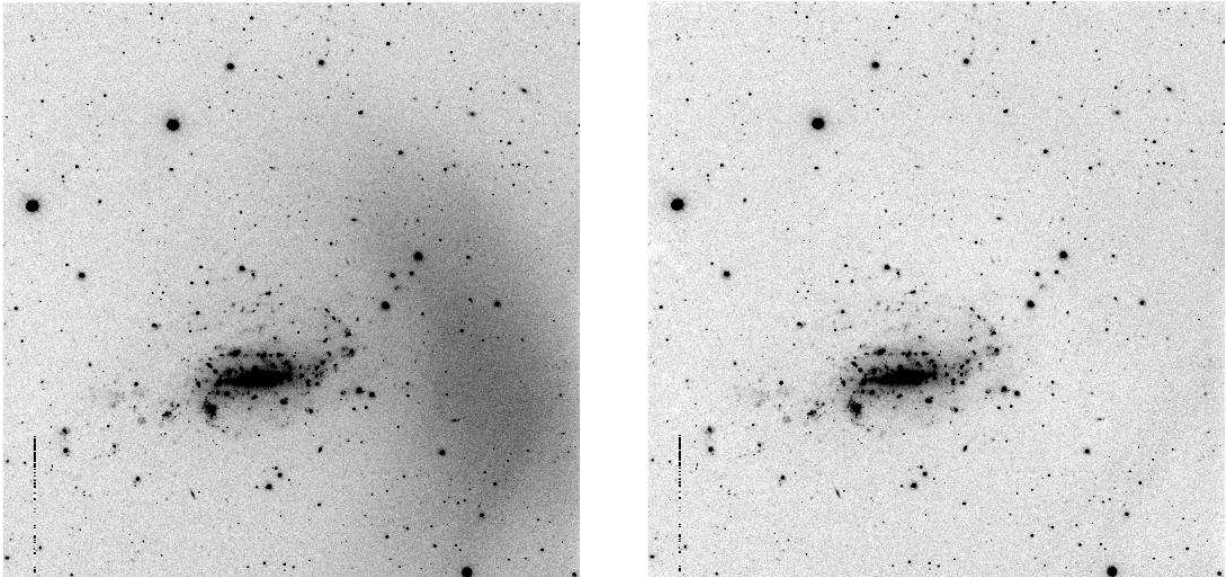


FIG. 3.— A single flat-fielded 6568/28 exposure of HiPASS J0459-26 displayed with an inverse linear stretch showing the “hump” instrumental artifact (left), and after hump removal (right). These images were created using the same stretch after applying a 3×3 median filter followed by a 4×4 block average in order to reject cosmic rays and enhance the appearance of smooth features such as the hump.

sources have the highest count rate (excluding very short exposures and saturated images). The header of this file becomes the basis of that of the output image.

Continuum subtraction is performed using the algorithm given by Alard (2000). The frame with the best seeing is convolved with a kernel that matches it to the PSF of the frame with the worst seeing, and the scaled continuum image is subtracted from the NB frame. The flux scaling is implemented by setting the sum of the convolution kernel to the appropriate scale factor.

3.6. Astrometric calibration

SE catalogs were matched to the U.S. Naval Observatory A2.0 database (Monet et al. 1998). Typically, on the order of 100 sources were matched resulting in an rms accuracy of $\sim 0.4''$ (about one pixel) to the coordinate system zeropoint.

3.7. Source identification

Identification of Emission Line Galaxies (ELGs) was done visually using color composite images. These were created using the R image in the blue channel, the NB image in the green channel and the net $H\alpha$ image in the red channel, resulting in emission line sources appearing red. This assignment is used in all color images presented here. The display levels are scaled to the noise level in the frames allowing sources to be discerned to a consistent significance level in all images. We define an ELG to be a discrete source that is noticeably extended in at least the R -band and contains at least one emission line source. This phenomenological definition is deliberately broad and allows an extended galaxy with one unresolved HII region to be considered an ELG.

The aim is to find any star-forming galaxies associated with the HI source. However, we can not be certain

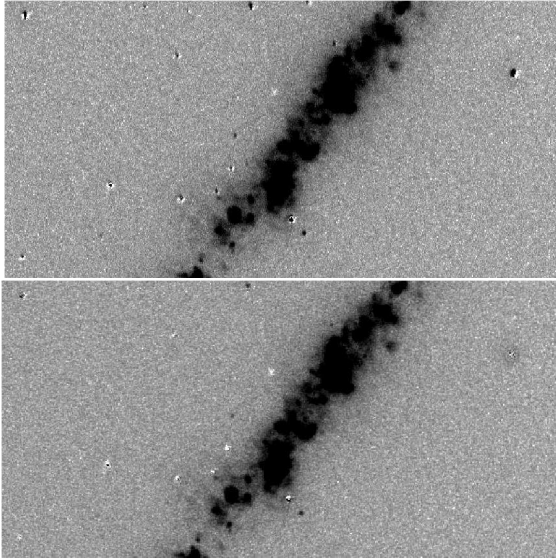


FIG. 4.— A section of the R subtracted image of HiPASS J2052-69. Top: “traditional” processing; Bottom “High- z supernova” software processing. The two methods are outlined in Sec. 3.5.

that the ELGs correspond to the location of HI within the Parkes beam. Similarly, we could also detect background sources in some other emission line redshifted into the passband of the NB filter (e.g. [O III]5007Å, H β , or [O II]3727Å at $z \sim 0.3, 0.4,$ and 0.8 respectively). Further spectroscopic and HI imaging follow-up would be required to unequivocally determine which ELGs are associated with the HiPASS sources. Despite these concerns, the rich morphology of extended distributions of HII region in the vast majority of the ELGs is consistent with them being associated with the HiPASS targets.

We also frequently find emission line sources that are unresolved or barely resolved in both the R and NB images and projected far from any apparent host galaxies. We classified these sources as “ELDots” which is a phenomenological shorthand description for their appearance - Emission Line Dots. The nature of the ELDots is not immediately apparent; they could be outlying HII regions in the targeted galaxy, or background line emitters. Ryan-Weber et al. (2004) obtained optical spectra of 13 ELDots with the ANU 2.3m telescope and confirmed the detection of line emission of five in the field of three HiPASS galaxies (HiPASSJ0209–10, HiPASSJ0409–56, and HiPASSJ2352–52). For four of the five ELDots, H α was detected at the systemic velocity of the HiPASS galaxy, while in the fifth case (HiPASSJ2352–52) only one line was detected, at a wavelength outside that expected for H α at the systemic velocity. The majority of the eight ELDots not detected spectroscopically were probably fainter than the detection limit of the observations (Ryan-Weber et al. 2004). Additional ELDots in the SR1 images presented here are in the process of being cataloged and confirmed (J. Werk et al., in preparation).

3.8. Sky subtraction

We determine the sky level in an annulus around the galaxy that is set interactively. We use color images to define the brightness peak as well as four points that specify the major and minor axes of the aperture that

encompasses all the apparent emission in both H α and the R band. In most cases this aperture has a shape and orientation close to that of the outer R band isophotes. In cases where a minor axis outflow is readily apparent in H α , the aperture is made rounder in shape to accommodate the outflow. Galaxies with such an outflow are discussed in Appendix B. For galaxies with a few small scattered HII regions at large radii, we typically match the aperture in size and shape to the outer R band isophotes, leaving some HII regions outside of this aperture. The semi-major axis size r_{sky} parameterizes the inner size of the sky annulus. Next, r_{sky} is tweaked using crude radial surface brightness profiles; the images are divided into 35×35 pixel boxes, the 3σ clipped mean level of each box is plotted as a function of semi-major axis distance, and the distance at which the mean intensity levels off in both the net H α and R band images is selected as the new r_{sky} . In some cases there are slight radial gradients in the sky, due to scattered light, and the mean intensity level does not level off. In those cases we do not reset r_{sky} . The outer sky radius is set so that the sky annulus has an area equal to that interior to r_{sky} . The exceptions are very large galaxies, where the available sky area is limited by the CCD boundaries, and small galaxies, where we set the minimum area to 16 arcmin². The sky level is the 3σ clipped average of the mean level in each box wholly within the sky annulus, rejecting boxes that have had pixels rejected in the clipping within the box. The pixel-to-pixel noise of each image is taken to be the average clipped rms values within the boxes. The large scale (> 35 pixels) uncertainty in the sky is taken as the dispersion in the mean levels in the boxes used to define the sky; this represents the uncertainty due to imperfect flat-fielding and scattered light.

3.9. Image masking

We use two types of masks, exclusion and inclusion, to indicate how to use pixels when integrating fluxes. These masks rely heavily on SE catalogs as well as “segmentation images” produced by SE which indicate which source each pixel belongs to.

For the R and NB images, the exclusion mask uses the position, SE flag values, source size, stellarity parameter (star/galaxy classification), flux, and R /NB flux ratio to identify the pixels to exclude. The SE segmentation image is displayed, and allows interactive toggling of which sources are masked or kept. To make the final exclusion mask, this mask is grown by convolving it with a circular top hat function with a radius equal to the seeing width (or a minimum of $1.2''$) so that the fringes of unrelated stars and galaxies are also rejected. The net H α image requires less exclusion masking, because most of the faint foreground and background sources are adequately removed with continuum subtraction. Our algorithm uses the uncertainty in the continuum scaling ratio to determine which pixels masked in the R -band are likely to have residuals greater than 1.5 times the pixel-pixel sky noise. In addition, we exclude pixels corresponding to concave sources resulting from residuals around bright stars. The bad pixels are grown as described above to make the final H α exclusion mask.

The inclusion mask is needed primarily to account for HII regions that are detached from the main body of a galaxy. In many cases, a simple aperture that is large

enough to include all of a large galaxy’s HII regions would result in a sky uncertainty that is so big that the derived total flux would be meaningless. The inclusion mask is based on an SE analysis of the net H α image. We use a logic similar to that adopted to find sources that are most likely foreground, background, or artifacts, and take all other sources to be part of the galaxy being measured. The grow radius of the inclusion mask is twice the seeing width or a minimum of 2.4’’.

The algorithm for defining the masks is straight forward but not perfect. Objects at the edge of frames, satellite trail residuals, and the wings of bright stars are sometimes mistakenly placed in inclusion masks, while occasionally portions of the target galaxy, such as line-free knots, are excluded. Therefore, each set of masks were examined by two of us (G.R.M. and D.J.H.). This was done by examining color images of (a) the entire field, (b) only the pixels included in total R band flux measurements, (c) only the pixels not included in total R flux measurements, (d) only the pixels included in the net H α flux, and (e) only the pixels not included in the total H α flux. These images were compared to determine if there were regions that should or shouldn’t be included in the masks. Mistakenly excluded or included SE sources were toggled. In some cases circular or polygon shaped areas were added as needed to the masks to insure that the measurements recover as much of the true flux while excluding obvious contaminating features.

3.10. Measurements

The ideal way to measure total H α fluxes is to just use a simple aperture (e.g. circular or elliptical) that is large enough to encompass all HII emission. In addition to being easy to specify, this technique has the advantage of including all emission in the aperture, including that from faint HII regions and Diffuse Ionized Gas (DIG) that may be below the apparent detection limit of the observations. In contrast, measuring H α fluxes by summing the light from HII regions typically underestimates the true flux by 30% – 50% because of the neglected DIG (Ferguson et al. 1996; Hoopes, et al. 2001; Helmboldt et al. 2004). However, as alluded to above, using large apertures may result in very low S/N due to the sky uncertainty over the very large aperture needed to contain the outermost HII regions. We have developed a hybrid approach that uses the sum of the aperture flux where the S/N level is reasonable, supplemented with the flux of HII regions outside of this aperture that are within the inclusion mask described above. The method is similar in concept to that employed by Ferguson et al. (1998).

Surface brightness and curve of growth (enclosed flux) profiles are extracted for each source using concentric, constant shape elliptical apertures. The shape and centers of the apertures are the same as those set in the sky determination. The difference in flux between apertures defines the surface brightness profile. The curve of growth profiles are corrected for the excluded pixels in each annulus by adding the missing area times the mean unmasked intensity in the annulus. In the majority of ELGs (96 of 111) the curve of growth plateaus at or very close r_{sky} , and we terminate the profiles at a maximum radius $r_{\text{max}} = r_{\text{sky}}$. In some cases the profiles plateau inwards of r_{sky} , or the S/N of the enclosed flux is low.

Hence, our adopted algorithm for determining r_{max} is to use the smallest of (a) where the curve of growth flattens, (b) r_{sky} , or (c) where $S/N = 3$. Here the noise is crudely estimated from the large scale sky variation (Sec. 3.8; as discussed in Sec. 4.3 below, this overestimates the error in the enclosed flux, hence the actual S/N is higher). Beyond r_{max} , we still include the flux of pixels indicated by the inclusion mask in our total flux measurements. Figure 5 shows an example of how pixels are masked and which pixels are included when measuring total H α fluxes.

We find some H α flux outside of r_{max} in 30% of the ELGs studied here. However, in most cases the fractional H α flux outside of r_{max} is negligible; it is greater than 0.1, 0.05, 0.01 in 3, 6, and 16 cases respectively. The most extreme case is HiPASS J1217+00 (Fig. 5) where 41% of $F_{\text{H}\alpha}$ is beyond r_{max} .

The curve of growth is interpolated to determine the effective radius r_e , the radius along the semi-major axis containing half the flux and from this the face-on effective surface brightness, defined as

$$S_e = \frac{F}{2\pi r_e^2} \quad (2)$$

where F is the total flux of the target¹⁶. We are primarily concerned with the effective surface brightness of H α , $S_e(\text{H}\alpha)$. We also calculate the effective surface brightness in the R -band which we convert to the ABmag scale yielding $\mu_e(R)$. Using the same algorithm, we also calculate r_{90} , the radius containing 90% of the total flux and do not calculate this value if more than 10% of the flux is beyond r_{max} .

The equivalent width we use is that within the H α effective radius, $r_e(\text{H}\alpha)$, and is given by

$$EW_{50} = \frac{0.5F_{\text{H}\alpha}}{f_R(r_e(\text{H}\alpha))} \quad (3)$$

where $f_R(r_e(\text{H}\alpha))$ is the R -band flux density per wavelength interval within $r_e(\text{H}\alpha)$. It is derived from the R -band aperture photometry and the standard definition of fluxes in the ABmag system. We use EW_{50} instead of a total equivalent width since it is directly comparable to $S_e(\text{H}\alpha)$, which is also measured within $r_e(\text{H}\alpha)$. In addition, EW_{50} usually has considerably smaller errors due to the smaller aperture area needed for the measurement.

For each ELG, two sets of radial profiles are made, one where the extraction apertures are centered on the brightness peak, the other where the apertures are centered on the geometric center of the outermost apparent isophote. We use the former set to define r_e , and the latter set to define the total flux, r_{90} and r_{max} .

We found the above method to be sufficient to perform the measurements in all but two cases, shown in Fig. 6, which we now detail. **HiPASS J0403–01**: the field of this galaxy is strongly contaminated with H α emitted by Galactic cirrus; in addition there is a bright star very near the target galaxy. Because of its presence, we observed the galaxy with the 6850/95 filter instead of the R band, so as to minimize saturation. The galaxy is seen primarily by the presence of a few HII regions located

¹⁶ the face-on correction occurs because r_e is a semi-major axis length, and thus πr_e^2 is the face-on area provided the generally elliptical isophotes result from a tilted disk.

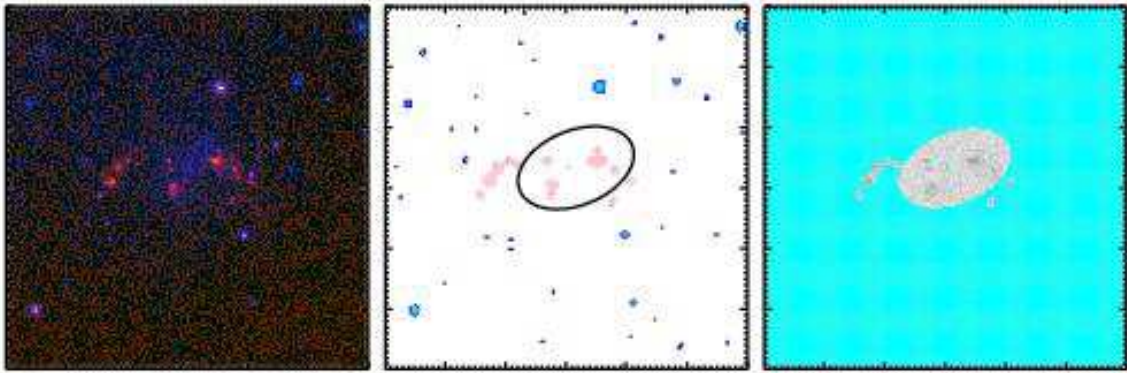


FIG. 5.— Steps involved in image masking and total flux measurement. The left panel shows a 600×600 pixel subsection of the HiPASS J1217+00 image in color using our standard assignment: red - net $H\alpha$ emission; green - NB image (no continuum subtraction); and blue R (continuum). The middle panel indicates pixels masked as stars, or stellar residuals in the R and net $H\alpha$ marked blue and cyan respectively, which comprise the exclusion mask; and pixels identified as dominated by $H\alpha$ marked pink, the inclusion mask. The ellipse indicates the aperture having r_{\max} . The right hand panel shows a grayscale of the net $H\alpha$ image. Pixels that are not used in the total $H\alpha$ flux calculation are colored cyan.

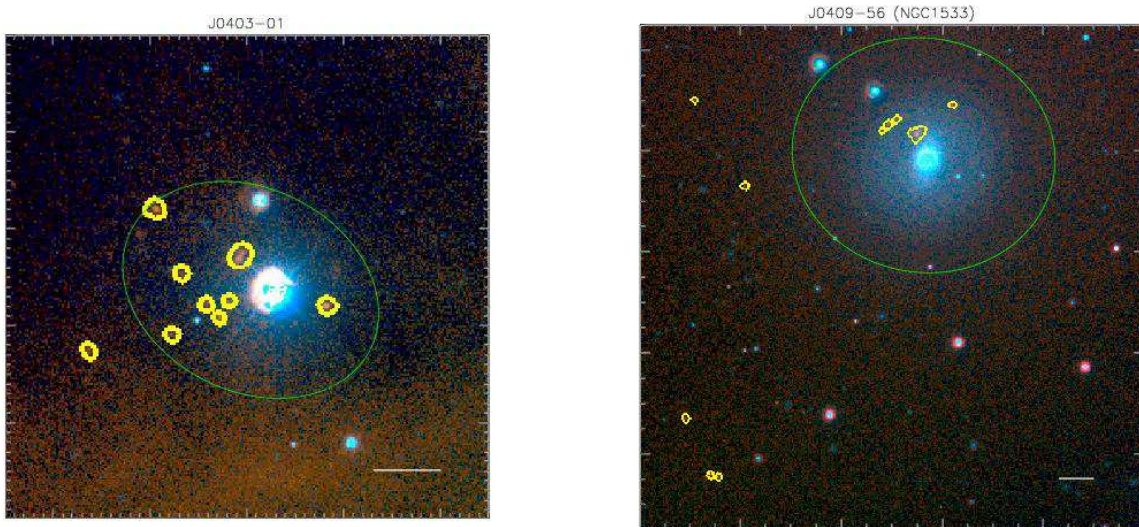


FIG. 6.— Color, partial frame images of HiPASS J0403–01 (left) and HiPASS J0409–56 (right) with net $H\alpha$, narrow band (not continuum subtracted), and 6850/95 displayed in red, green, and blue, respectively. The apertures used to measure the $H\alpha$ flux are outlined in yellow, while the aperture used to measure the total 6850/95 flux is shown in green. The scale bar (lower right each panel) is $30''$ long.

near the bright star. If there is diffuse $H\alpha$ it can not be disentangled from the foreground cirrus. We therefore measure $F_{H\alpha}$ using the summed flux from the HII regions, measured with small apertures placed around each source. It is not clear whether the galaxy is detected in the continuum due to the glare from the bright star. We use an elliptical aperture whose center is offset from the bright star to measure the continuum flux. The center of the bright star is masked from the aperture, but we were not able to remove the light from the outskirts of the star. The measured continuum flux should be considered an upper limit. **HiPASS J0409–56** (NGC 1533) is a high-surface brightness SB0 galaxy. The center of this galaxy is saturated in the R band so we used images through the 6850/95 filter to obtain the continuum flux. A few HII regions as well as the ELDots discussed by Ryan-Weber et al. (2004) are visible in the net $H\alpha$ image. The continuum is so strong relative to $H\alpha$ in this galaxy that the $F_{H\alpha}$ derived using our standard technique is to-

tally swamped by the continuum subtraction uncertainty. As for the case of HiPASS J0403–01 we measure $F_{H\alpha}$ through a set of eye-selected small apertures centered on the HII regions, as well as the ELDots (since they were shown to be part of the galaxy by Ryan-Weber et al. 2004). The continuum flux is measured through a large elliptical aperture, as is usually the case. The reader is cautioned that for both these cases the apertures used to measure $F_{H\alpha}$ and the continuum flux are considerably different. Since $F_{H\alpha}$ measures only the light of the noticeable HII regions it may be significantly underestimated in these cases. We have not attempted to measure $r_e(H\alpha)$, r_{90} , and related quantities, in them because of the unorthodox nature of the measurement aperture.

3.11. Flux corrections

Line fluxes are corrected for the effects of foreground and internal dust absorption, $[N II]$ contamination, and underlying $H\alpha$ absorption. R -band fluxes are corrected

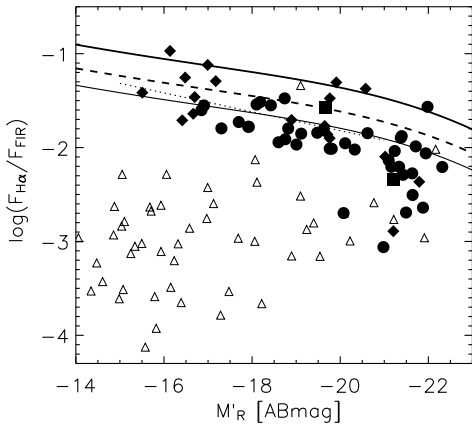


FIG. 7.— Comparison of the H α to FIR flux ratio, $F_{\text{H}\alpha}/F_{\text{FIR}}$, with the R -band absolute magnitude (with no internal extinction correction) M'_R . IRAS data were used to derive the FIR flux using the algorithm of Helou et al. (1988). Filled symbols mark IRAS detections with the data taken from the IRAS large optical galaxy catalog (Rice et al. 1988), the IRAS Faint Source Catalog (Moshir et al. 1990), and the IRAS Point Source Catalog marked with squares, diamonds, and circles respectively. Triangles correspond to sources which are not in any of these catalogs. We take these to be non-detections by IRAS and place them at their 3σ lower limits in $F_{\text{H}\alpha}/F_{\text{FIR}}$. The curves represent the application of simple dust reprocessing models on stellar population models as discussed in the text, with the main difference being in the IMF. The solid line is for a Salpeter (1955) IMF which has a slope $\alpha = 2.35$, and a mass range of $1 - 100 M_{\odot}$; the dashed line is for $\alpha = 2.35$ over the mass range of 1 to $30 M_{\odot}$. The thin solid line and dotted line segment show fits to the data having $M'_R > -21$ ABmag: the thick solid line shifted vertically and a simple linear fit respectively.

for foreground and internal dust.

The foreground dust absorption is parameterized by the reddening $E(B - V)$ taken from the Schlegel, Finkbeiner & Davis (1998) maps and listed in Table 3. The extinction at the observed wavelength of H α is calculated using the extinction law of Cardelli, Clayton & Mathis (1989). For the average $V_h = 2000 \text{ km s}^{-1}$ of the full SINGG sample H α is at an observed $\lambda = 6606.6 \text{ \AA}$ and the foreground Galactic extinction is $A_{\text{H}\alpha, \text{G}} = 2.50E(B - V)$. For the R -band we adopt a foreground dust absorption of $A_{\text{R}, \text{G}} = 2.54E(B - V)$.

To correct for internal dust, we adopt the relationship used by Helmboldt et al. (2004) between the Balmer decrement ($F_{\text{H}\alpha}/F_{\text{H}\beta}$) derived internal dust absorption $A_{\text{H}\alpha, \text{i}}$ and the R -band absolute magnitude calculated *without* any internal dust absorption correction M'_R . This is based on Balmer line ratios measured from integrated (drift scan) galaxy spectra of the Nearby Field Galaxy Survey (Jansen 2000; Jansen et al. 2000). After correcting to the AB magnitude system, the internal dust absorption is given by:

$$\log(A_{\text{H}\alpha, \text{i}}) = (-0.12 \pm 0.048)M'_R + (-2.47 \pm 0.95) \quad (4)$$

The radiation that dust absorbs is re-emitted in the far-infrared (FIR). Hence FIR observations can provide a valuable test of the $A_{\text{H}\alpha, \text{i}}$ correction. In Fig. 7, we use IRAS $60\mu\text{m}$ and $100\mu\text{m}$ flux densities to calculate the “total” $40\text{-}120\mu\text{m}$ flux F_{FIR} using the formula given by Helou et al. (1988). The IRAS data are taken from three sources as noted in the caption to Fig. 7. 61/113 SR1 ELGs are detected by IRAS, in the remaining cases

we show the ratio at the 3σ upper limit to their F_{FIR} flux. The IRAS detected ELGs do show a trend of decreasing $F_{\text{H}\alpha}/F_{\text{FIR}}$ with decreasing M'_R , while the non-detections are consistent with the trend.

To test whether the trend is consistent with eq. 4 we apply a simple model for the dust extinction and re-emission in the infrared. In it, a stellar population is enshrouded in dust that obeys the Calzetti, et al. (2000) dust obscuration law. The amount of gas phase extinction is parameterized by $A_{\text{H}\alpha, \text{i}}$ derived from M'_R using eq. 4. The flux absorbed by the dust is re-emitted in the FIR and we assume that 71% of the dust emission is recovered by F_{FIR} (Meurer, Heckman, & Calzetti 1999). We show curves for two models and two fits to the data. For the models, the stellar populations are solar metallicity 100 Myr duration continuous star formation models from Starburst99 (Leitherer et al. 1999). They differ only in their IMF which is parameterized by a single power law in mass having slope $\alpha = 2.35$ (Salpeter 1955) and a specified mass range, a lower mass limit of $1 M_{\odot}$, and an upper mass limit m_u of $100 M_{\odot}$ (solid line) and $30 M_{\odot}$ (dashed line). The H α output in photons per second is taken to be 46% of the ionizing photon output, as expected for case B recombination of an ionization limited HII region. Neither of these models passes through the center of the observed ratios of the detected sources, although the $m_u = 100 M_{\odot}$ model nicely defines the upper envelope. Adopting $m_u = 30 M_{\odot}$ results in a better match, but is still displaced with respect to the data. We also tested a model with a steeper $\alpha = -3.3$ and $m_u = 100 M_{\odot}$. It has the same shape and falls between the other two models. We omit showing it so as not to clutter the figure.

In order to better understand the correlation we make two fits. In the dot dashed curve we take the $m_u = 100 M_{\odot}$ model and fit the best offset in the y -axis finding it to be -0.43 dex, while the thin solid line shows a simple linear fit. For both cases we are only fitting the data for galaxies with $M'_R > -21$; we use a robust fitting algorithm and reject outliers. The rms dispersion in the $\log(F_{\text{H}\alpha}/F_{\text{FIR}})$ residuals about the fits are 0.22 dex for the linear fit, and 0.23 dex for the shifted model. The fits both yield a reasonable representation of the data for $M'_R > -21$, while the galaxies with $M'_R \leq -21$ have an average displacement of -0.25 dex from the offset model fit.

The *shape* of the model curves is driven by the form of the $A_{\text{H}\alpha, \text{i}}$ versus M'_R relationship. We see that the adopted model adequately specifies the shape, except for the brightest galaxies. This can be seen by the fairly good agreement of the linear fit and the shifted model line. However, the model does not adequately account for the *zeropoint* of the relationship, instead an arbitrary shift is required. The zeropoint of the model effectively gives the ratio of the ionizing to bolometric flux of the stellar populations. As noted above, adjusting m_u or α can shift the model lines vertically. An error in the stellar models themselves can also result in a zeropoint error. Recent improvements in the modeling of hot stars using non-LTE expanding atmospheres with realistic line blanketing (Smith et al. 2002; Martins et al. 2005) indicate that the ionizing flux output of stars is lower than expected from the Lejeune et al. (1997) stellar atmosphere models used by Starburst99, resulting in

our model $F_{\text{H}\alpha}/F_{\text{FIR}}$ values being too high. The use of improved stellar models should then move the model lines in the correct direction. It is also possible that older populations could also contribute significantly to the dust heating, but not the ionization. These could result from a star formation history that is declining with time. This would be in the correct sense compared to compilations of the cosmic SFR density evolution (e.g. Pérez-González et al. 2005; Glazebrook, et al. 2003). Finally, the offset could be due to the inadequacy of the dust model to account for all star formation. Then, the fact that our Balmer-decrement based models don't recover this star formation would indicate that it is totally hidden by dust.

Our model adequately models the trend of the $\text{H}\alpha$ extinction for galaxies having $M'_R > -21$ ABmag, but is not capable of self-consistently accounting for the FIR emission. The SINGG ELGs that have been detected by IRAS are on average 2.7, 4.8 times brighter in the FIR than predicted by our model for galaxies less and more luminous than $M'_R = -21$ ABmag respectively. As noted above there are a variety of explanations for this offset. If the zeropoint offset is removed, then at the faint end, our dust absorption model predicts the $F_{\text{H}\alpha}/F_{\text{FIR}}$ ratio, and by inference the SFR, to within an a factor of 1.7. This is sufficient for our purposes - we wish to determine star formation rates that can be inferred from $\text{H}\alpha$ fluxes and quantities that can be inferred from optical wavelength observations. Recovery of the star formation that is totally obscured by dust, is beyond the scope of this survey. Our adopted dust absorption model is conservative in that it does not over-predict the FIR emission.

Since HII regions represent star formation sites, where dust and gas concentrations are particularly strong, they represent enhanced dust absorption compared to that seen in the older stellar populations in the galaxy. Indeed, it has long been known that internal extinction estimates of galaxies derived from Balmer lines are larger than those found by continuum fitting, typically by a factor of ~ 2 (Fanelli, O'Connell, & Thuan 1988; Calzetti, Kinney & Storchi-Bergman 1994). Therefore we adopt $A_{R,i} = 0.5A_{\text{H}\alpha,i}$ to correct M'_R to the total (internal and foreground) dust corrected absolute magnitude M_R .

To correct for [N II] contamination we adopt the correlation between the [N II] line strength and M'_R given by Helmboldt et al. (2004) and corrected to the ABmag system

$$\log(w_{6583}) = (-0.13 \pm 0.035)M'_R + (-3.30 \pm 0.89) \quad (5)$$

where

$$w_{6583} \equiv \frac{F_{[\text{NII}]6583\text{\AA}}}{F_{\text{H}\alpha}} \quad (6)$$

As before, the correlation is based on the NFGS sample of Jansen (2000). The correction of the line flux includes both [N II] lines at 6583Å and 6548Å and is calculated using the filter profile and a simple emission line velocity profile model as outlined in Appendix A.

An important source of possible bias results from $\text{H}\alpha$ emission being hidden by $\text{H}\alpha$ absorption. McCall et al. (1985) found a typical Balmer line absorption EW of 1.9Å in a wide range of extragalactic HII regions. HII

regions represent active sites of star formation, and typically have a high equivalent width and small covering factor over the face of a galaxy. What we need is a correction for $\text{H}\alpha$ absorption appropriate to the integrated spectra of galaxies. For this we turn to the SDSS, whose fiber spectra typically account for one third of the flux in nearby galaxies, as shown by B04. They show that adopting a uniform $\text{H}\alpha$ absorption correction corresponding to $EW(\text{H}\alpha)_{\text{absorption}} = 2\text{\AA}$ could cause systematic errors in SFR determinations with stellar mass. They note typically the stellar absorption comprises 2% – 6% that of the stellar emission in flux. Therefore we uniformly increase $F_{\text{H}\alpha}$ and $EW(\text{H}\alpha)$ by 4% to account for underlying stellar absorption.

A correction to the photometry of the three sources observed with the 6850/95 narrow band continuum filter was applied in order to make their magnitudes compatible with those in the R band. We found that the fluxes for the two cases where the source were observed with both filters have identical flux density *per wavelength interval* f_λ (within the errors) derived from each filter. Since the two filters have different pivot wavelengths (Table 5) their flux density *per frequency interval*, and hence ABmag differs. For a flat f_λ spectrum, the correction to add to $m_{6850/95}$ in ABmag to get the equivalent m_R is $5 \log(6858.9/6575.5) = 0.114$ mag, which we apply to all $m_{6850/95}$ measurements.

Finally we note some effects that we have not corrected for. (1) We have not corrected our R -band fluxes for contamination by $\text{H}\alpha$ or other emission lines ([N II], [S II] and [O I] typically being the strongest). Since we find a median $EW_{50}(\text{H}\alpha) = 16\text{\AA}$ and the width of the R filter is 1450 Å (Table 5), then the R fluxes will typically be underestimated by a few percent. This in turn means that EW_{50} will also be underestimated by a few percent. The galaxies with the highest EW_{50} would require the largest corrections, up to $\sim 25\%$. (2) Changes in the NB filter transmission curves due to temperature changes and filter aging may cause errors in $\text{H}\alpha$ fluxes. Neither effect has been calibrated, but we expect the errors to be limited to the few percent level.

4. GLOBAL PROPERTIES DATABASE

The results of the image analysis are listed in Tables 6, 7 and 8. Combined, these represent the tabulated data of SR1. In all tables, the first column gives the source designation used in this study. If there is only one ELG in the field the HiPASS designation is used. If there is more than one, the HiPASS name is appended with “:S1”, “:S2”, etc. in order to distinguish the sources, where the “S” stands for SINGG. Table 6 defines the apertures used to measure fluxes, presents the identification of the sources from catalog matching, and provides morphological information from a variety of literature sources. The optical identifications were adopted from HOPCAT, (the HiPASS optical catalog of Doyle et al. 2005), the BGC, or from the NASA/IPAC Extragalactic Database (NED¹⁷). There are four ELGs in SR1 with no previously cataloged optical counterparts: HiPASS J0403–01

¹⁷ The NASA/IPAC Extragalactic Database (NED) is operated by the Jet Propulsion Laboratory, California Institute of Technology, under contract with the National Aeronautics and Space Administration.

(also noted by Ryan-Weber et al. 2002); HiPASS J0503-63:S2; HiPASS J0504-16:S2, and HiPASS J1131-02:S3.

Table 7 presents the measured properties of the sources. These include the R band absolute magnitude M_R ; the effective and 90% enclosed flux radii in the R band, $r_e(R)$, $r_{90}(R)$; the corresponding quantities in net $H\alpha$: $r_e(H\alpha)$, $r_{90}(H\alpha)$; the $H\alpha$ derived SFR; the face-on star formation rate per unit area, within $r_e(H\alpha)$, SFA; the face-on R band surface brightness within $r_e(R)$, $\mu_{e,0}(R)$; and the $H\alpha$ equivalent width within $r_e(H\alpha)$, $EW_{50,0}$. These are intrinsic properties, that is corrected for Galactic and internal extinction and in physically meaningful units. We also present $H\alpha$ fluxes, $F_{H\alpha}$, corrected only for internal extinction and [NII] contamination to allow easy comparison with other work (e.g. Helmboldt et al. 2004; James et al. 2004; Marlowe et al. 1997). In Table 7 the star formation rates given by SFR and SFA have been calculated using the conversion $SFR [1M_\odot \text{ yr}^{-1}] = L_{H\alpha} [\text{erg cm}^{-2} \text{ s}^{-1}] / 1.26 \times 10^{41}$ calculated by Kennicutt, Tamblyn, & Congdon (1994), and adopted by many other studies (e.g. Kennicutt 1998; Lee et al. 2002; Kodama et al. 2004; Hopkins 2004; Helmboldt et al. 2004). This conversion adopts a Salpeter (1955) IMF slope with lower and upper mass limits of 0.1 and $100 M_\odot$. To compare our results to those that adopt the Kroupa (2001) IMF, as do some more recent studies (Kauffmann et al. 2003; Tremonti et al. 2004, e.g. B04;), one should divide our SFR estimates by 1.5 (B04). The errors presented in Table 7 are derived from the error model discussed in Sec. 4.3, below. The corrections adopted and discussed in Sec. 3.11 are given in Table 8.

Full frame color representations of the images are presented in Figure 8. The NB image has a larger display range than the net $H\alpha$ image, resulting in the HII regions appearing orange-red with yellow or white cores. The paper version of this article shows only a portion of Fig. 8. All images are available in the online version of this article.

4.1. Image quality

The quality of the net $H\alpha$ and R band images is specified by the seeing, the limiting flux, and the flatness of the sky. The limiting EW is an additional quality measurement that is only applicable to the net $H\alpha$ images. Statistics on these quantities are compiled in Table 9, for both the net $H\alpha$ images, and where relevant, the R band images as well. Histogram plots of these quantities are shown in Figures 9 and 10 for the net $H\alpha$ images.

The FWHM seeing values (Fig. 9a) are mostly less than $2''$, with a median of $1.6''$. The seeing values are slightly worse in net $H\alpha$, since our method results in the net image having the larger seeing of those in R and NB.

The limiting flux, f_{lim} is derived from

$$f_{\text{lim}} = n_\sigma \sigma f_{\text{ap}} \sqrt{\pi r_{\text{seeing}}^2 / a_{\text{pix}}} \quad (7)$$

where σ is the pixel-to-pixel rms of the background, r_{seeing} is the seeing radius (half the FWHM seeing plotted in Fig 9a), $a_{\text{pix}} = 0.19 \text{ arcsec}^2$ is the pixel area, f_{ap} is the aperture correction within r_{seeing} (we adopt $f_{\text{ap}} = 2.0$), and $n_\sigma = 5$ is the adopted significance level of the limiting flux. Defined this way, f_{lim} is the n_σ limiting flux of a point source detection. Figure 9b plots the histogram

of f_{lim} . The median limiting $H\alpha$ flux corresponds to a luminosity $L_{H\alpha} \sim 10^{37} \text{ erg s}^{-1}$ (neglecting any extinction corrections) at the median distance of the SINGG sample. This corresponds to about half the ionizing output of a single O5V star (solar metallicity) using the ionizing flux scale of Smith et al. (2002).

The sky flatness, σ_S , is a traditional estimate of the quality of an image. It is defined as the *large scale* variation in the background. We measure σ_S as the rms of the background measurements in 35×35 pixel boxes in the sky annulus. Hence, this is a measurement of local flatness, rather than a full frame measurement (except for the largest sources). Histograms of σ_S are displayed in $\text{erg cm}^{-2} \text{ s}^{-1} \text{ arcsec}^{-2}$ in Fig. 9c. Emission line surface brightness is often given in other units: Rayleighs, defined as $\mathcal{R} = 10^6 / 4\pi \text{ photons cm}^{-2} \text{ s}^{-1} \text{ sr}^{-1} = 5.67 \times 10^{-18} \text{ erg cm}^{-2} \text{ s}^{-1} \text{ arcsec}^{-2}$, and emission measure $EM = 2.78 \times \mathcal{R} \text{ pc cm}^{-6}$ for an assumed electron temperature $T_e = 10^4 \text{ K}$. In these units the median large scale (area $\gtrsim 15'' \times 15''$) rms surface brightness variations in the net $H\alpha$ images corresponds to $0.51\mathcal{R}$ and $EM = 1.4 \text{ pc cm}^{-6}$. This is about sixty times fainter than the surface brightness cut used by Ferguson et al. (1996) to define DIG emission. In Sec 4.3 we parameterize the uncertainty due to sky subtraction as a function of σ_S .

The dispersion in the narrow band to R band scaling ratio, σ_{rat} , for background and foreground sources can be used to estimate the range of intrinsic EW values of sources that are not line emitters, σ_{EW} . We define this quantity as

$$\sigma_{EW} = \sigma_{\text{rat}} \frac{U_{\text{NB,line}}}{U_R}. \quad (8)$$

Here, $U_{\text{NB,line}}$ is the unit response to line emission in the NB frame and U_R is the unit response to the continuum flux density in the R image. These quantities are defined in Appendix A. The quantity σ_{rat} is the dispersion about the mean of the NB to continuum flux ratio, derived from matched sources in the SE catalogs of the frames, after applying a three sigma clip to the ratios. Figure 10 shows that σ_{EW} is lowest for the two SINGG filters which have a median $\sigma_{EW} = 2.4\text{\AA}$. The MCELS 6568/28 has a significantly higher median $\sigma_{EW} = 3.2\text{\AA}$ probably because this filter encompasses Galactic $H\alpha$. The NOAO filters have the highest median $\sigma_{EW} = 4.5\text{\AA}$ due to their broader bandpass widths. In Sec 4.3 we demonstrate that the mean flux scaling ratio can be determined to significantly better than σ_{EW} . However, measured $EW(H\alpha)$ values approaching σ_{EW} should be treated with some caution because differences between the flux scaling of program sources versus foreground and background sources could result in systematic errors approaching σ_{EW} .

4.2. Quality assurance tests and rejected images

We subjected the images and our database to a wide range of quality assurance tests. As noted in Sec. 2.4, our sample was checked for possible HVC contamination, and uniform HI properties were adopted. The reality of all tentative low S/N $H\alpha$ detections (in terms of flux or EW) as well as multiple ELGs was checked by eye, resulting in the removal of some overly optimistic ELG identifications. Optical identifications were checked in cases where our identification did not agree with HOPCAT.

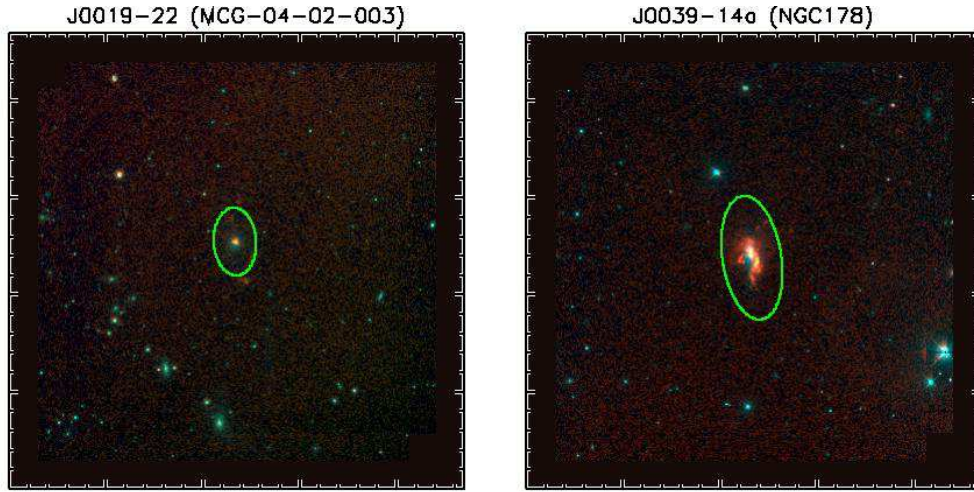


FIG. 8.— (*Sample portion of figure.*) Three color images of the target fields, with net $H\alpha$, narrow band (not continuum subtracted), and R displayed in red, green, and blue, respectively. North is up, east is to the left, and the tick marks are separated by 100 pixels ($43''$). HiPASS names and optical identifications are given above each frame. The elliptical flux measurement aperture is shown in green. For fields with multiple sources they are labeled with the SINGG ID (S1, S2, etc.).

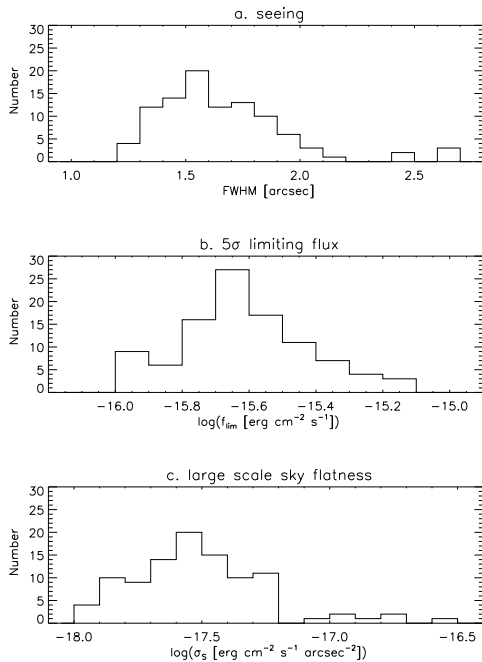


FIG. 9.— Histograms of net $H\alpha$ image quality measurements. Panel a. (top): FWHM seeing; b. (middle) 5σ limiting flux; and c. (bottom) large scale ($\sim 15''$) sky flatness.

The radial profiles and curves of growth were checked for the effects of unmasked or improperly masked objects. We calculated the fraction of the unmasked image covered by the HiPASS half-power beam area for the HiPASS source that was targeted. We also checked that the filter used for the observation covered the velocity of the source. Color images of all sources were examined to check source location, large scale sky variations, and other blemishes. Cases where the source extends to the edge of the frame or beyond are marked in Table 7.

These tests revealed four sets of observations which we rejected as non-survey observations. These include observations of a source rejected from our final sample (it is

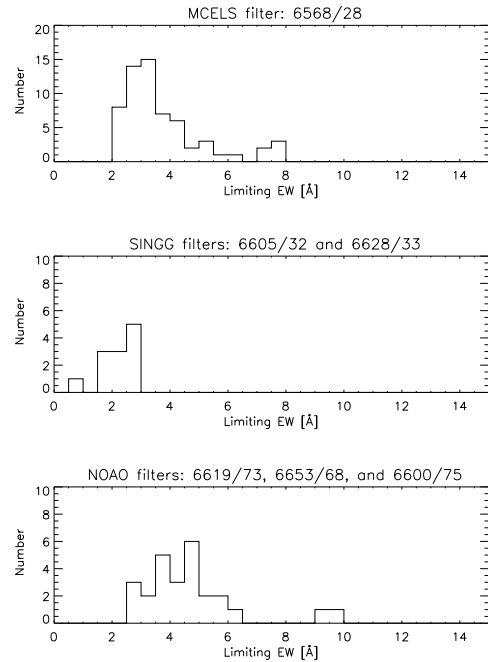


FIG. 10.— The scatter in the NB to R (or 6850/95) ratio within a frame calibrated to an EW using eq. 8. σ_{EW} is derived from SE catalogs and represents the typical uncertainty in a single foreground or background source.

part of the Magellanic stream), two cases of mis-pointing due to HI position errors in earlier versions of our sample selection, and one observation set that was rejected due to a very bright sky background ($10\times$ normal due to the proximity of the gibbous Moon). In this paper we use these observations only to define our sky error model in the following subsection.

4.3. Error model

In measurements of extended sources, typically the largest sources of random error are sky subtraction, which affects both the R and $H\alpha$ results, and continuum subtraction which affects the $H\alpha$ results. These affect not

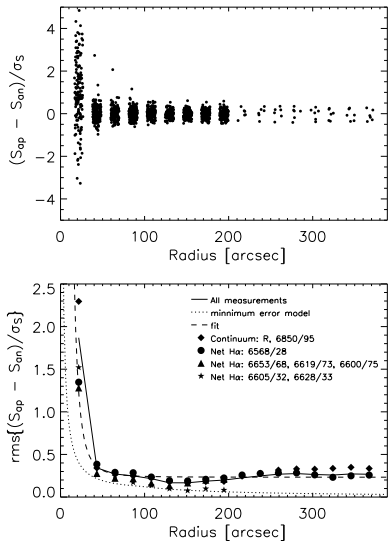


FIG. 11.— Derivation of the sky uncertainty model. The top panel shows the sky level difference between that within a circular aperture and that in the surrounding sky annulus, normalized by σ_S the dispersion in sky measurements within the sky annulus. The data were measured in blank portions of real data frames, and are plotted against aperture radius, r . Small random offsets in r are employed in this plot to allow the density of the measurements to be distinguished. The measurements for $r > 200''$ were performed on frames containing no ELGs. The bottom panel shows the rms dispersion of the quantity above. The solid line uses all measurements at each r in determining the mean, while the symbols are for different subsets of filters as noted in the legend. The dotted line shows the “least sky error” model, while the dashed line shows our fit to the combined measurements.

only the fluxes but also the other measurements obtained here. The rest of this subsection details our error model for these terms. In addition there is a flux calibration error. We have adopted a calibration error of 0.04 mag for data obtained with the 6568/28 filter and 0.02 mag for data obtained with the other filters, which was derived from the residuals of the observed minus intrinsic magnitude versus airmass of the standard stars. Since the data presented here span several observing runs and filters, this error term is considered to be a random error and is added in quadrature with the other flux uncertainties described below.

By measuring the sky in an annulus around the source, we can estimate the sky within r_{sky} more accurately than the large scale sky fluctuations σ_S which we use to characterize the flatness of the image. To demonstrate and calibrate this effect we placed apertures, of a variety of sizes, on “blank” portions of our images - that is in areas away from the target sources. This allows the sky to be measured in both the sky annulus and interior to r_{sky} . These tests were restricted to circular apertures; there is no reason to expect the results to differ for elliptical apertures of equivalent area.

The results are shown in Fig. 11. The top panel plots the difference in sky levels interior to r_{sky} and that in the annulus normalized by σ_S . For $r_{\text{sky}} \geq 50''$, the difference in sky values is typically less than the large scale sky fluctuations. The points at $r_{\text{sky}} = 50''$ in the top panel of Fig. 11 have a mean value somewhat offset from zero, implying that the sky is systematically higher in the measurement aperture than the sky annulus. This probably results from a difference in the sky determina-

tion algorithm we had to implement for apertures this small. For large r_{sky} we use our standard clipping algorithm (Sec 3.8) to determine the sky level in both the sky annulus and interior to r_{sky} . However, $r_{\text{sky}} = 50''$ is so small that often too few 35×35 pixel boxes survive to accurately measure the sky level. Hence, in this case we take the sky interior to r_{sky} to be simply the 3σ clipped mean of all the pixels within the aperture. Since there is no box rejection, the measurement can include the wings of some stars, and hence may be slightly elevated.

The bottom panel shows the rms of the normalized sky difference measurements. We take this quantity to be equivalent to ϵ_S/σ_S where ϵ_S is the true sky uncertainty within the measurement aperture (this approximation somewhat overestimates ϵ_S since some of the rms can be attributed to the uncertainty in the sky level within the sky annulus). We show this quantity for cases where we combine all measurements at each radius to calculate the rms, and when we consider continuum images separately from net H α images which are further subdivided into logical filter groups. The dotted line shows a “least sky error” model. This would be applicable if the overall sky was flat and residual sky errors occurred on scale sizes less than the 35 pixel box size used to make the sky measurements. For this model

$$\frac{\epsilon_S}{\sigma_S} = \sqrt{\frac{N_{\text{ap}} + N_{\text{an}}}{N_{\text{ap}}N_{\text{an}}}}, \quad (9)$$

where N_{ap} and N_{an} are the number of measurement boxes within r_{sky} and the sky annulus respectively. The dotted line is drawn assuming perfect packing of the boxes and none rejected. The fact that almost all measurements are above this line indicates that residual sky errors typically have scale sizes larger than 35 pixels. The dashed line shows our fit to the data

$$\frac{\epsilon_S}{\sigma_S} \approx 0.23 + \left(\frac{22.5''}{r}\right)^3. \quad (10)$$

This is an “eye” fit to the data adopted for convenience of calculation, and is not meant to provide insight to the origins of the residual sky errors. When applying this model to the elliptical apertures used in the actual galaxy measurements we replace r with the equivalent radius, \sqrt{ab} , where a and b are the semi-major and semi-minor axes dimensions of the flux measurement aperture. To determine the total flux error due to the sky, we multiply the model by σ_S in units of count rate per pixel and the aperture area in pixels and calibrate to yield the total flux error due to sky in the appropriate units. We adopt a maximum $\epsilon_S/\sigma_S = 2$ to avoid the model blowing up at small r .

To translate this to uncertainties in r_e , r_{90} and S_e we derive what the curve of growth would be if the sky level was changed by adding or subtracting ϵ_S . This results in two additional curves of growth. The r_e , r_{90} and S_e values are found as before resulting in two additional estimates of these quantities. We then find the maximum difference in these quantities between three estimates - that derived from the nominal curve of growth and those derived from the additional curves of growth. We take the error to be one half this maximum difference.

The random uncertainty on H α flux measurements due to continuum subtraction is set by how well the adopted

continuum scaling ratio is determined. Since many foreground and background sources are used to determine this ratio, we expect the accuracy to be better than the source to source rms in the flux ratio σ_{rat} (defined in Sec 3.10). Since the NB filters and continuum filters have similar mean wavelengths, and to first order the spectral properties of foreground and background sources should not vary significantly from field to field at the high latitudes of our survey, then we take the fractional error due to continuum subtraction, ϵ_C/C to be the field to field dispersion in the continuum scaling ratio normalized by the mean continuum ratio. The adopted values of ϵ_C/C are given in Table 5. They range from 0.024 to 0.043, about one third of σ_{rat} . We made sufficient observations to determine the normalized rms for four NB filters. For two other NB filters (6628/33 and 6600/75) we have not made enough observations to determine an accurate rms (we require at least four), and so adopt the fractional continuum error from similar filters. The $H\alpha$ flux error within an aperture is then determined by multiplying the continuum count rate C by ϵ_C/C to get the count rate uncertainty. This is then multiplied by the flux scaling coefficient to get the $H\alpha$ flux uncertainty. The errors on r_e , r_{90} and S_e due to continuum subtraction are found in a method analogous to the sky error. The errors due to continuum subtraction and that due to sky subtraction are added in quadrature to yield the total random error on the $H\alpha$ flux. We derive the uncertainty on $EW_{50,0}$ by propagating the flux errors in $H\alpha$ and R band within $r_e(H\alpha)$.

4.4. Tests of the error model

To test the internal accuracy of our error model we use repeat measurements: We repeated observations in three cases albeit with slightly different filters. In each case, one of the two measurements was superior, and that was adopted in the measurements given in Table 7. Nevertheless, the other set was of sufficient quality to test our error model. We now briefly discuss the results and note which observation was chosen for our results. Measurements given in these comparisons have not been corrected for internal extinction. **HIPASS J0507-7** (NGC 1808) was observed with both the R and 6850/95 filters in run 01 as a test of the accuracy of narrow band continuum subtraction. Using an extraction aperture $r_{\text{max}} = 6'$ we measure the quantities $[r_e, r_{90}, m, \mu_e]$ for the R and 6850/95 observations of $[70.0 \pm 0.8, 213 \pm 7, 9.451 \pm 0.025, 20.592 \pm 0.023]$ and $[67.1 \pm 1.7, 197 \pm 15, 9.496 \pm 0.036, 20.547 \pm 0.033]$ respectively (in units of [arcsec, arcsec, ABmag, ABmag arcsec $^{-2}$]). Hence, the difference between the observations are $[2.8 \pm 1.8, 17 \pm 17, 0.044 \pm 0.043, 0.045 \pm 0.40]$ - all within about 1.5σ of zero. The R band observations are centered better on the galaxy than the 6850/95 images. They also have higher S/N and this clearly shows in the smaller errors above, hence we adopt the R image for our final measurements. **HIPASS J0409-56** (NGC 1533) was observed with the 6850/95 filters in run 01 after realizing that R images were saturated in the nucleus. For this reason we adopt the 6850/95 results for our published measurements. Using a broad annulus from $r = 9''$ to $240''$ (in order to avoid the saturated nucleus), we measure $m_R = 10.476 \pm 0.021$ ABmag and $m_{6850/95} = 10.504 \pm 0.066$ ABmag, yielding a magnitude

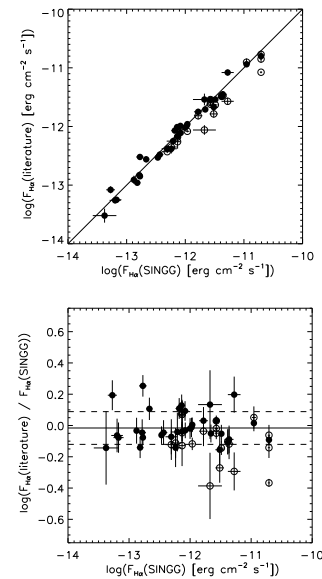


FIG. 12.— Comparison of our total $H\alpha$ fluxes with values from the literature (open circles) and from the HUGS group (Kennicutt et al. 2006, in preparation, filled circles). The top panel plots fluxes from other sources against ours. The solid line is the unity relationship. The bottom panel plots the ratio of fluxes from other sources to our own, compared to the SINGG flux. The solid line marks the mean using only the HUGS data. The dashed lines indicate the $\pm 1\sigma = 0.104$ dex dispersion about the mean HUGS value. The sources for the published $F_{H\alpha}$ values are Gil de Paz et al. (2003); Hoopes, et al. (2001); Hunter, Hawley, & Gallagher (1993); Hunter et al. (1994); Hunter & Elmegreen (2004); Marlowe et al. (1997); Martin (1998); Moustakas & Kennicutt (2006), and Ryder & Dopita (1994).

difference of 0.028 ± 0.033 , or zero within errors. Because of the saturation in R , we have not compared half or 90% enclosed light quantities. **HIPASS J0943-05b** (UGCA 175) was observed with two different NB filters on separate nights of run 02. The first set of observations with the 6600/75 filter have an elongated PSF due to poor tracking. The second set of images obtained with the 6619/73 filter have a superior PSF and results from it are used as our adopted measurements. Using our adopted extraction aperture $r_{\text{max}} = 1.66'$ we measure $[r_e(H\alpha), r_{90}(H\alpha), \log(F_{H\alpha}), \log(S_e(H\alpha))] = [33.8 \pm 2.9, 67.3 \pm 3.6, -12.33 \pm 0.08, -16.19 \pm 0.13]$ and $[33.3 \pm 2.5, 66.2 \pm 1.8, -12.36 \pm 0.08, -16.21 \pm 0.13]$ with the 6600/75 and 6619/73 images respectively (in units of [arcsec, arcsec, $\log(\text{erg cm}^{-2} \text{ s}^{-1})$, $\log(\text{erg cm}^{-2} \text{ s}^{-1} \text{ arcsec}^{-2})$). Hence the difference between the filters for these quantities are $[0.4 \pm 3.9, 1.1 \pm 4.0, 0.03 \pm 0.12, 0.02 \pm 0.18]$; again the results agree within the errors.

As an external check of our fluxes, Fig. 12 compares our total $\log(F_{H\alpha})$ measurements with a variety of published measurements as well as with measurements from 11HUGS (11 Mpc $H\alpha$ and UV Galaxy Survey, Kennicutt et al. 2006, in preparation). 11HUGS has completed an $H\alpha$ and R -band imaging survey of an approximately volume-limited sample of ~ 350 spiral and irregular galaxies within a distance of 11Mpc. The comparisons in Fig. 12 are made as close to “raw” values as possible in order to reduce the possible sources of error. We correct the $F_{H\alpha}$ for [N II] contamination, because NB filter transmission curves vary strongly from survey to survey, but almost always transmit some [N II]. No internal extinc-

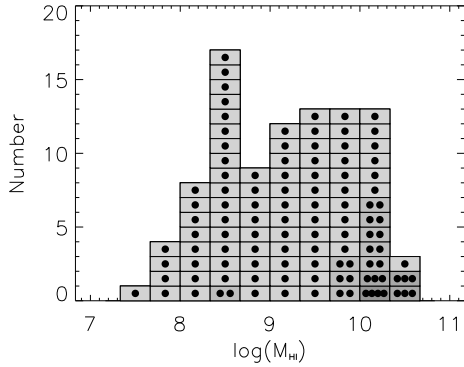


FIG. 13.— The HI mass histogram of the 93 SR1 targets. Each rectangle represents one HiPASS target, while each dot within a rectangle represents an Emission Line Galaxy (ELG).

tion, nor $H\alpha$ absorption corrections were applied. Likewise we have not attempted to exactly match apertures with the literature or HUGS measurements. The errors are taken from the publications, where available, otherwise we adopt a mean error of 0.063 dex, derived from the SINGG $F_{H\alpha}$ used in the plot. The bottom panel compares the logarithmic ratio of the published $F_{H\alpha}$ fluxes to the SINGG value plotted against the SINGG flux. Hence the errors are the x and y errors in the top panel added in quadrature.

The weighted mean $\log(F_{H\alpha}(\text{literature})/F_{H\alpha}(\text{SINGG})) = -0.030$ with a dispersion of 0.12 dex, when using all 56 measurements. Concentrating on just the 34 HUGS measurements yields a weighted mean $\log(F_{H\alpha}(\text{literature})/F_{H\alpha}(\text{SINGG})) = -0.016$ and a scatter of 0.10 dex. We conclude that the SINGG $H\alpha$ fluxes agree well with other measurements - to within 33% on average. The agreement is a bit better, to within 27% for galaxies in common with the recent HUGS survey. For an average error of 16% from SINGG and 12% from HUGS we expect a scatter of 0.08 dex about the mean. While our error model can account for much of the measured variance an additional $\sim 11\%$ flux uncertainty (added in quadrature) in both the SINGG and HUGS fluxes would be required for a full accounting. Possible sources of additional error include aperture placement, flux calibration (particularly in the filter transmission curves and flux standards), and the [N II] correction.

5. RESULTS

5.1. $H\alpha$ detectability of HI-selected galaxies

Figure 13 shows the HI mass histogram of the 93 SR1 targets. In this histogram, each box represents a single HiPASS source. Each dot within a box indicates a discrete $H\alpha$ emitting galaxy as defined in Sec. 3.7. Thus some HiPASS sources contain multiple ELGs, while all SR1 targets contain at least one ELG. This does not mean that all HI rich galaxies are also star forming. Later (non SR1) SINGG observations have uncovered at least one HiPASS galaxy that is undetected in $H\alpha$ despite deep $H\alpha$ observations. The present study shows that high-mass star formation is highly correlated with the presence of HI, and that HI rich but non-star-forming galaxies are rare.

The high detectability of HI sources in $H\alpha$ is remarkable. Recently Doyle et al. (2005) showed that there are no “dark” (optically invisible) HI galaxies among the 3692 HICAT sources with low foreground Galactic extinction, bolstering earlier claims that starless galaxies are rare (Zwaan et al. 1997; Ryan-Weber et al. 2002). The dearth of dark HI galaxies may be due to the fact that when there is sufficient HI for a gas cloud to be self gravitating, it is gravitationally unstable until newly formed stars and supernovae heat the ISM enough to arrest further star formation. Thus an HI cloud that is massive enough to be self-gravitating is likely to have already formed at least some stars, and hence should be visible. Star formation should set in at a lower HI mass if there is already some matter (e.g. dark matter) available to bind the ISM. Low-mass HI clouds that are not self-gravitating would have low column density and would be susceptible to ionization by the UV background (Zwaan et al. 1997). HI is therefore either associated with stars or destroyed. The theory behind this scenario is studied in detail by Taylor & Webster (2005) who conclude that galaxies with baryonic masses $\gtrsim 5 \times 10^6 M_{\odot}$ should be unstable to star formation and hence not be dark.

Our results allow a stronger statement - gas bearing dormant galaxies are rare. That is, if a galaxy has an ISM with $M_{\text{HI}} \gtrsim 3 \times 10^7 M_{\odot}$, then it almost always has *recently* (within 10 Myr) formed high-mass stars. The gravitational instability in the ISM is not halted globally by feedback from evolved stellar populations. Instead, new stars continue to form, including the massive stars that ionize HII regions.

5.2. Range of Properties

The SINGG ELGs cover a wide range of properties, as shown by the histograms in Fig. 14. These show the distribution of the properties before (shaded histogram) and after internal dust absorption correction (solid line). We caution the reader that these are measured distributions of the detected ELGs, and do not necessarily easily transform into true volume averaged number densities. While we do make some comparisons with other samples, the aim is to show the diversity of the ELGs, rather than to quantify differences with other samples.

Figure 14a shows the histogram of R absolute magnitudes, which is a crude measure of the stellar content of the sources. The distribution is broad, covering four orders of magnitude in luminosity, with no strong peaks. We find ELGs ranging from $M_{R,0} = -13.1$ (corresponding to HiPASS J1131-02:S3, a barely extended anonymous ELG) to $M_{R,0} = -23.1$ (HiPASS J2202-20:S1 = NGC 7184); that is from well in the dwarf galaxy regime to nearly two magnitudes brighter than the knee in the R -band luminosity function $M_*(R) = -21.5$ (found from interpolating the SDSS luminosity functions of Blanton, et al. 2003).

The $H\alpha$ luminosity, $L_{H\alpha}$, is our basic measurement of the star formation rate. The $L_{H\alpha}$ distribution, shown in Fig. 14b, covers about four orders of magnitude in luminosity and has no strong peaks. It ranges from $\log(L_{H\alpha}) = 38.2 \text{ erg cm}^{-2} \text{ s}^{-1}$ (HiPASS J0043-22 = IC 1574) to $\log(L_{H\alpha}) = 42.25 \text{ erg cm}^{-2} \text{ s}^{-1}$ (HiPASS J0224-24 = NGC 922), corresponding to a star formation rate of 0.0012 to $14 M_{\odot} \text{ yr}^{-1}$. None of the SR1

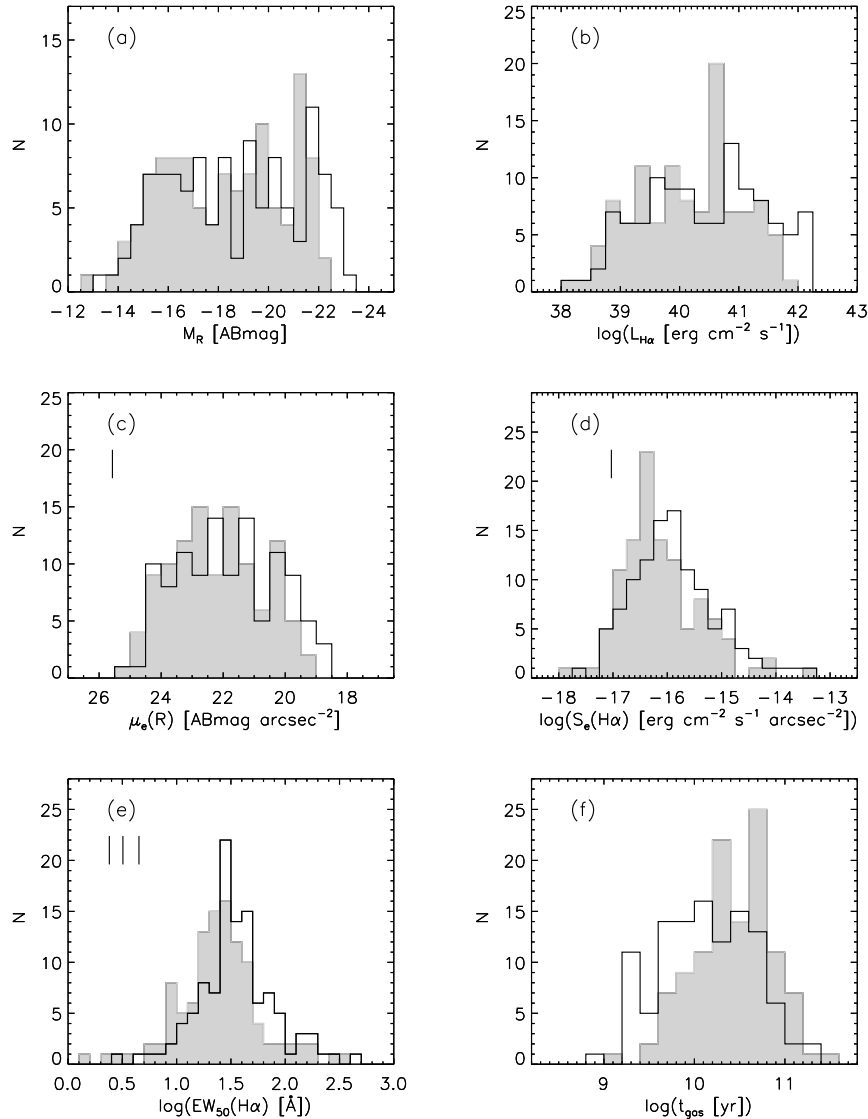


FIG. 14.— Histogram of ELG observed properties. In all panels, the gray shaded histogram shows the distribution of quantities with no internal dust extinction correction, while the black line shows the quantities with internal dust corrections. Panel (a) shows the R -band absolute magnitude M_R distribution. Panel (b) shows the $H\alpha$ luminosity $L_{H\alpha}$ distribution. Panel (c) shows the R -band effective surface brightness $\mu_e(R)$ distribution. The tick mark shows the average $3\sigma_S$ where σ_S is the large scale sky variation. Panel (d) shows the $H\alpha$ effective surface brightness $S_e(H\alpha)$ distribution. The tick mark shows the average $3\sigma_S$. Panel (e) shows the effective $H\alpha$ equivalent width EW distribution. The tick marks indicate the median σ_{EW} (eq. 8) or the NB SINGG filters, the MCELS 6568/28 filter, and the 75\AA wide NOAO filters. Panel (f) shows the distribution of the gas cycling timescale t_{gas} .

ELGs has a star formation rate approaching that of an ultraluminous infrared galaxy, of $\sim 150 M_{\odot} \text{ yr}^{-1}$. The ionizing output of the weakest ELG corresponds to ionization by 7 O5V stars (Smith et al. 2002).

The R -band face-on effective surface brightness, $\mu_e(R)$, gives the integrated surface density of stars. The distribution, shown in Fig. 14c, spans about 3.5 orders of magnitude in intensity (surface brightness), ranging from $\mu_e(R) = 25.2 \text{ ABmag arcsec}^{-2}$ (HiPASS J1106–14, an LSB dwarf irregular galaxy) to $18.6 \text{ ABmag arcsec}^{-2}$ (HiPASS J0209–10:S2 = NGC 838, a starburst galaxy in a compact group). The distribution is broad with a sharp drop at the low surface brightness end. The edge is near the detection limit of our data, so may represent a bias. If the ELGs contain a lower surface brightness component, we would not be able to detect it.

The ELGs typically have lower surface brightness than the low redshift galaxies targeted for spectroscopy by the Sloan Digital Sky Survey (SDSS). This is illustrated in Fig. 15 which compares the cumulative histograms in $\mu_e(R)$ for the SINGG ELGs and a sample of 2.8×10^4 low redshift SDSS galaxies cataloged by Blanton et al. (2005). The latter catalog includes SDSS spectroscopic sample targets weeded of portions of larger galaxies that were incorrectly identified as separate sources. From their published catalog we calculated μ_e in the SDSS r' and i' passbands using the Petrosian flux and half light radii. We then interpolated these to the effective wavelength of the Harris R filter to obtain $\mu_e(R)$. Both the SINGG and Blanton et al. (2005) samples have been corrected for Galactic extinction but not internal extinction in this plot. The inter-quartile range of the Blanton

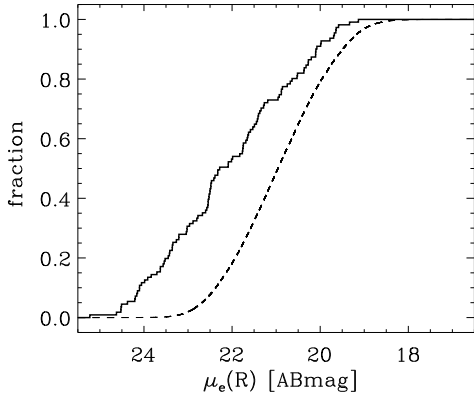


FIG. 15.— Cumulative histograms of R -band face-on effective surface brightness, $\mu_e(R)$, of the SINGG ELGs (thick solid line) and the sample of about 28,000 SDSS spectroscopic targets cataloged by Blanton et al. (2005, thin dashed line). We derived $\mu_e(R)$ from their cataloged quantities as described in the text.

et al sample is 21.75 to 20.16 ABmag arcsec⁻² significantly narrower and brighter than that of the SINGG ELGs: 23.30 to 20.91 ABmag arcsec⁻². Blanton et al. (2005) note that the deficit of the lowest surface brightness galaxies ($\mu_e(r') > 23.5$ mag arcsec⁻²) in their catalog is largely a result of their software for selection of sources for spectroscopy. Kniazev et al. (2004) demonstrate that significantly lower intensity sources can indeed be found in the SDSS images.

The H α effective surface brightness indicates the intensity of star formation, that is the rate of star formation per unit area. This is the key observable quantity to test any model where the energetic output of star formation balances the hydro-static pressure of the disk ISM (e.g. Kennicutt 1989). Heckman (2005) argues that the most physically important distinguishing characteristic of starburst galaxies is their very high star formation intensities. The observed distribution, shown in Fig. 14d, spans 4.4 orders of magnitude, ranging from $\log(S_e(\text{H}\alpha)) = -17.69$ erg cm⁻² s⁻¹ arcsec⁻² to $\log(S_e(\text{H}\alpha)) = -13.31$ erg cm⁻² s⁻¹ arcsec⁻². This corresponds to a range in star formation intensity, Σ_{SFR} , from 8×10^{-5} to $2.0 \mathcal{M}_{\odot}$ kpc⁻² yr⁻¹. The least intense detected star-formation occurs in HiPASS J1106–14, while the most intense star formation occurs in HiPASS J1339–31A (NGC 5253), a well known starburst dwarf galaxy (or blue compact dwarf; e.g. Calzetti et al. 1997). The low surface brightness end of the distribution corresponds to the approximate detection limit of the data, indicating that there may be lower surface brightness emission that we are missing.

EW_{50} indicates the star formation rate compared to the past average. Figure 14e shows that for the cases where this is defined it ranges from 2.8Å for HiPASS J0514–61:S1 (or ESO119-G048 an SBa galaxy)¹⁸ to 451 Å (HiPASS J1339–31A), for the sources detected in H α . While the lowest EW_{50} measurements are likely to be highly uncertain due to continuum subtraction, the distribution is peaked, centered at $EW_{50} \approx 24$ Å well be-

¹⁸ It is possible that HiPASS J0409–56 has a lower EW_{50} , but in this case we can not accurately measure EW_{50} due to the strength of its continuum

yond the detection limits of the data. Using the models of Kennicutt, Tamblyn, & Congdon (1994) and the adopted IMF this corresponds to a birthrate parameter $b \approx 0.2$, where b is the ratio of current star formation to the past average.

Figure 14f plots the histogram of gas cycling time t_{gas} , which we define to be:

$$t_{\text{gas}} \approx 2.3 \left(\frac{\mathcal{M}_{\text{HI}}}{\text{SFR}} \right). \quad (11)$$

Here the factor 2.3 corrects the HI mass for helium content and the expected mean molecular content of galaxies. The latter was derived from the optically-selected sample of galaxies observed by Young et al. (1996) which has $\langle \mathcal{M}_{\text{H}_2} / \mathcal{M}_{\text{HI}} \rangle = -0.06$ with a dispersion of 0.58 dex. We approximate this as equal masses in molecular and neutral components. t_{gas} estimates how long star formation at its present rate would take to process the observed neutral and inferred molecular phases of the ISM. Hence t_{gas} is an estimate of the future potential of star formation. t_{gas} ranges from 0.7 Gyr (HiPASS J1339–31A, again) to 220 Gyr (HiPASS J0409–56), that is, from starburst like timescales to many times the Hubble time $t_H = 13.5$ Gyr ($H_0 = 70$ km s⁻¹ Mpc⁻¹, $\Omega_M = 0.3$, $\Omega_{\lambda} = 0.7$). Figure 14f shows that the t_{gas} distribution is broad, with 41% of the sample having $t_{\text{gas}} < t_H$.

Figure 14 shows that our adopted internal dust absorption corrections have a modest impact on the observed distributions. In general, the dust correction spreads out the histograms.

The SINGG ELGs exhibit diverse morphologies. They include spirals (e.g. HiPASS J1954–58 = IC 4901) and later type systems (e.g. HiPASS J0459–26 = NGC 1744), but also residual star formation in Sa and S0 systems (e.g. HiPASS J0409–56). Irregular galaxies are well represented in the sample from low surface brightness dwarf irregulars with just a few HII regions (e.g. HiPASS J0310–39 = ESO300-G016) to high-surface brightness windy blue compact dwarf (e.g. HiPASS J1339–31A). The sample also includes interacting systems (e.g. HiPASS J0209–10 = four members of HCG 16) and mergers (e.g. HiPASS J0355–42 = NGC 1487). The H α images often enhance structures that are relatively subtle in broad band images thus revealing information on the dynamics of the system. These include small scale inner rings, large outer rings (HiPASS J0403–43:S1 = NGC 1512, for example, has both), bars (e.g. HiPASS J0430–01 = UGC 3070) and spiral arms (e.g. HiPASS J0512–39 = UGCA106). In other cases the structures that are apparent in the R -band are less obvious in H α (e.g. HiPASS J2334–36 = IC 5332 shows a grand-design spiral structure in R and an apparent random HII region distribution in H α).

While most of our images reveal only a single ELG, multiple ELGs were found in 13 pointings. In the most extreme case, HiPASS J0209–10 (Hickson Compact Group 16) four ELGs were detected in a single frame. Thus the total number of ELGs in SR1 is 111, significantly larger than the number of fields observe. While in some cases the companions would have been recognized immediately at any optical wavelength (e.g. the two large spirals in HiPASS J2149–60), in many cases the companion is compact and has low luminosity, and hence could easily be mistaken for background sources

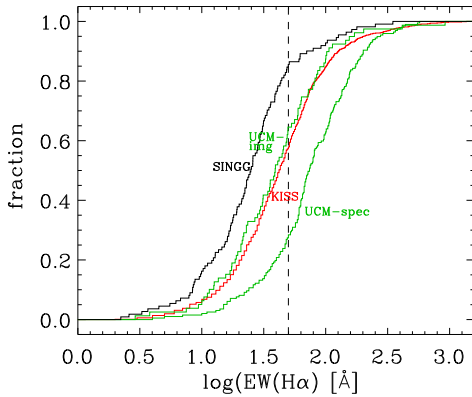


FIG. 16.— Cumulative histograms of $EW(H\alpha)$ for the SINGG SR1 ELGs (black line), and those from the KISS (red line) and UCM prism (green lines) surveys. For the SINGG galaxies, we plot EW_{50} . For the KISS survey we plot the prism $EW(H\alpha)$ values from Gronwall et al. (2004) while the UCM sample results for spectroscopically confirmed ELGs are shown from both spectroscopic data (UCM-spec, Gallego et al. 1996) as well as NB imaging data (UCM-img, Pérez-González et al. 2003). The dashed line marks the “traditional” starburst definition cut at $EW(H\alpha) \geq 50\text{\AA}$.

(e.g. HiPASS J0342–13:S2, and the dwarf member, S3, of the HiPASS J2149–60 system). This result demonstrates the value of $H\alpha$ imaging for identifying interacting companions with an unobtrusive appearance. Comments on the morphologies of all multiple ELGs can be found in Appendix B.

The wide range of star formation properties observed in our sample supports our contention that the SINGG survey is not strongly biased toward any particular type of star forming galaxy. This is not generally the case in star formation surveys. This is illustrated in Fig. 16 which shows the cumulative histogram of $EW(H\alpha)$ for SINGG compared to two prism based emission line surveys: KISS (Gronwall et al. 2004) and UCM (Gallego et al. 1996; Pérez-González et al. 2003). The prism-selected sources are weighted considerably more to high $EW(H\alpha)$ systems. This difference can not be attributed totally to how the $EW(H\alpha)$ measurements are made. $EW(H\alpha)$ measurements for the UCM survey were made from long-slit spectroscopic data (Gallego et al. 1996) as well as NB $H\alpha$ imaging (Pérez-González et al. 2003). The latter study was done to recover the “total” $H\alpha$ flux including that beyond the spectroscopic slit used by (Gallego et al. 1996). As shown in Fig. 16, the $EW(H\alpha)$ distribution in both UCM cases is skewed toward higher values than the SINGG sample. Taking the “traditional” definition of starbursts as having $EW(H\alpha) \geq 50\text{\AA}$, then 14%, 42%, 35%, and 72% of the SINGG, KISS, UCM imaging, and UCM spectroscopic surveys, respectively, are starbursts. Rather than SINGG missing out on starbursts, it is more likely that the prism surveys are missing low $EW(H\alpha)$ systems. Because we are not dealing with volume averaged densities in this comparison, it is premature to say how these differences translate into the relative biases of the surveys. That issue will be addressed further in paper II (Hanish et al. 2006).

6. CONCLUSIONS

The Survey for Ionization in Neutral Gas Galaxies (SINGG), is providing a view of star formation in the

local universe that is not hampered by the strong stellar luminosity based selection biases found in many other surveys. Our first results are based on observations of 93 of the total 468 HiPASS targets. These observations comprise the first release of SINGG data: SR1. All of these 93 targets contain $H\alpha$ Emission Line Galaxies (ELGs). The high detectability of star formation in HI rich galaxies confirms that HI is an important indicator of the presence of star formation. The detected galaxies cover a wide range of morphologies, including LSB spirals and irregulars, normal spirals, strong starburst activity with minor axis wind features, and residual star formation in early type disk systems. The ELGs we find have a $\mu_e(R)$ distribution extending to fainter intensities typically targeted for SDSS spectroscopy, while the EW_{50} distribution appears to be less biased toward starbursts than are prism surveys.

Multiple ELGs were found in 13 systems bringing the total number of ELGs imaged to 111. In many cases, the relationship between the companion and the primary source was not obvious from previous optical images. This illustrates how $H\alpha$ follow-up imaging is a valuable tool for identifying star forming companions to HI-selected galaxies.

This introduction to SINGG shows the potential for using a homogeneous HI-selected sample to explore star formation in the local universe. Other papers in this series will discuss the contribution of HI galaxies to the local cosmic star formation rate density (Hanish et al. 2006, paper II); the correlations between the global star formation properties of galaxies (Meurer et al. 2006); the HII region luminosity function and demographics of the diffuse ionized gas (DIG; Oey et al. in preparation); and the compact emission line sources projected far from their apparent hosts (the ELDots, J. Werk et al. in preparation). The SR1 data, both images and a database, are made available at <http://sungg.pha.jhu.edu/> for the benefit of other researchers and the public and as part of our commitment to the NOAO Surveys Program.

Partial financial support for the work presented here was obtained through grants from NASA including HST-GO-08201, HST-GO-08113, NAG5-8279 (ADP program), and NAG5-13083 (LTSA program) to G.R. Meurer; a Space Telescope Science Institute Director’s Discretionary Research Fund grant to H.C. Ferguson, NSF 0307386 and NASA NAG5-8426 to R.C. Kennicutt; an Australia Research Council Discovery Project - ARCD DP 0208618; NSF grant AST-0448893 to M.S. Oey; and NNG04GE47G (LTSA) to T. Heckman. The observations were made possible by a generous allocation of time from the Survey Program of the National Optical Astronomy Observatory (NOAO), which is operated by the Association of Universities for Research in Astronomy (AURA), Inc., under a cooperative agreement with the National Science Foundation. NOAO also supported this work with assistance in the purchase of two filters, support in scanning the filters at Tucson, as well as in excellent visitor support and hospitality at CTIO, La Serena and Tucson. At CTIO we received the expert assistance at the 1.5 m telescope from its operators: Alberto Alvarez, Mauricio Fernández, Roger Leighton, Hernan Tirado, and Patricio Ugarte, and especially for

the observer support work of Edgardo Cosgrove and Arturo Gómez. Our smooth operations are largely due to their skill and experience. We thank the NOAO Tucson filter experts - James DeVeney, Daryl Willmarth, Bill Blinkert, Bruce Bohannon and Heidi Yarborough, for scanning the filters and carefully performing other acceptance tests. We thank Arna Karick and Shay Holmes who assisted in obtaining the observations presented here. We are very thankful for data reduction assistance from Cheryl Pavlovsky (STScI) and Sanae Akiyama (U. Arizona) for performing initial CCD data reductions. The High- z Supernovae group assisted our efforts by providing access to their data reduction scripts. GRM is grateful for hospitality received during visits to the Australia Telescope National Facility Headquarters, the Univer-

sity of Melbourne, The University of Queensland, and the Australian National University's Mount Stromlo Observatory, were parts of this work were accomplished. We are thankful for useful conversations and correspondence with John Blakeslee, Holland Ford, Joe Helmboldt, Christy Tremonti, Linda Smith, Michael Blanton, and John Moustakas. We are grateful to the anonymous referee for comments and suggestions that have improved this paper. We thank Capella Meurer for suggestion of the SINGG acronym. This research has made use of the NASA/IPAC Extragalactic Database (NED) which is operated by the Jet Propulsion Laboratory, California Institute of Technology, under contract with the National Aeronautics and Space Administration.

Facilities: CTIO:1.5m

APPENDIX

FLUX CALIBRATION RELATIONS

Here we present the formalism for converting observed count rates to calibrated magnitudes and integrated $H\alpha$ line fluxes $F_{H\alpha}$. These relationships are easily derived using the principles of synthetic photometry (Bushouse & Simon 1998). We denote the count rate as $C_F(X)$ where the F subscript, used throughout this section, denotes the filter dependence. The airmass, X , dependence of the calibration is derived from the standard airmass equation:

$$m_{\text{true},F} - m_{\text{obs},F} = AX + B_F \quad (\text{A1})$$

where $m_{\text{true},F}$ is the true magnitude above the atmosphere and $m_{\text{obs},F} = -2.5 \log(C_F(X))$ is the observed magnitude. Because the filters used in this study all have similar central wavelengths, we simultaneously fit a single extinction term A (in units of mag airmass^{-1}) for all filters and individual zeropoints B_F for each filter. Typically a single night's worth of standard star observations were used in each fitting, although in periods of fine and stable weather we have been able to combine the data from several nights in a single fit.

Calibration is to spectro-photometric standards, and we use flux calibrated spectra of these stars to derive the true magnitude of the stars through the relevant filters. There are a variety of ways to define the true magnitude from a flux calibrated spectrum f_λ . For deriving the formulas here, the STmag system is most convenient

$$m_{\text{ST}} = -2.5 \log \langle f_\lambda \rangle - 21.1 \quad (\text{A2})$$

where $\langle f_\lambda \rangle$ is the bandpass averaged flux density (defined in eq. A5 below) and is in units of $\text{erg cm}^{-2} \text{s}^{-1} \text{\AA}^{-1}$. The magnitudes we quote here are in the more familiar ABmag system which is related to the STmag system by

$$m_{\text{AB}} = m_{\text{ST}} + 5 \log \left(\frac{5500}{\lambda_p} \right) \quad (\text{A3})$$

and λ_p is the pivot wavelength in \AA of the filter given by

$$\lambda_p = \sqrt{\frac{\int \lambda T_F(\lambda) d\lambda}{\int \lambda^{-1} T_F(\lambda) d\lambda}}. \quad (\text{A4})$$

Denoting the total system throughput as a function of wavelength $T_F(\lambda)$ then the mean flux density in the band is

$$\langle f_\lambda \rangle = \frac{\int \lambda T_F(\lambda) f_\lambda d\lambda}{\lambda_{m,F} W_{E,F}}. \quad (\text{A5})$$

Here f_λ is the spectrum of the source in $\text{erg cm}^{-2} \text{s}^{-1} \text{\AA}^{-1}$ and $\lambda_{m,F}$ and $W_{E,F}$ are the response weighted mean wavelength, and equivalent width of the passband given by

$$\lambda_{m,F} = \frac{\int \lambda T_F(\lambda) d\lambda}{\int T_F(\lambda) d\lambda} \quad (\text{A6})$$

and

$$W_{E,F} = \int T_F(\lambda) d\lambda. \quad (\text{A7})$$

Ideally $T_F(\lambda)$ should be the product of the CCD response, the throughput of all the optical elements (filters, primary and secondary mirrors), as well as the atmospheric transmission as a function of wavelength and airmass. For our purposes the standard extinction equation A1 is sufficient to remove the atmospheric response. Since there is very

little wavelength variation in the mirror coatings, we take $T_F(\lambda)$ to be the product of the filter and CCD responses. The unit response of a given observation is given by

$$U_F(X) = \frac{\langle f_\lambda \rangle}{C_F(X)}. \quad (\text{A8})$$

The airmass dependence is given by

$$\log \left(\frac{U_F(0)}{U_F(X)} \right) = -0.4AX. \quad (\text{A9})$$

where the unit response above the atmosphere is given by

$$\log U_F(0) = -0.4(21.1 + B_{F,ST}) \quad (\text{A10})$$

and $B_{F,ST}$ is the zeropoint from eq. A1 in the STmag system.

The unit response to line emission is defined to be

$$U_{F,\text{line}}(X) = \frac{C_{F,\text{line}}(X)}{F_{\text{line}}} \quad (\text{A11})$$

where F_{line} is the integrated line flux, in $\text{erg cm}^{-2} \text{ s}^{-1}$ and $C_{F,\text{line}}(X)$ is the count rate after continuum subtraction. $U_{F,\text{line}}(X)$ is given by

$$U_{F,\text{line}}(X) = U_F(X) \lambda_{m,F} W_{E,F} \frac{\int f_{\lambda,\text{line}} d\lambda}{\int \lambda f_{\lambda,\text{line}} T_F(\lambda) d\lambda} \quad (\text{A12})$$

where $f_{\lambda,\text{line}}$ is the emission line spectrum. For a single line this is the line profile, for multiple lines in the filter bandpass this is the summed profiles of all the lines. We experimented with various models for the line profile including δ function, Gaussian, and square function line profiles. Our adopted model is a Gaussian having the same V_h and W_{50} as the integrated H α profile:

$$G(\lambda_0, V_h, W_{50}, \lambda) = e^{-0.5x^2/\sigma^2} \quad (\text{A13})$$

where the peak amplitude is 1.0, λ_0 is the rest wavelength of the line and x and σ are given by the usual relationships $x = c(\lambda - \lambda_0)/\lambda_0 - V_{\text{hel}}$ and $W_{50} = \sqrt{8 \ln(2)}\sigma$, where σ is the Gaussian dispersion of the line. This model is meant to give a first approximation to the integrated H α velocity profile. While we do not know the H α velocity profile of the targets, we do know their H I profiles which are often Gaussian in shape in dwarf galaxies to double horn profiles for large spirals. As long as the profiles avoid the steep edges of the bandpass, we find that profile shape does not make a significant difference to the value calculated for $U_{F,\text{line}}$. Square profiles give $U_{F,\text{line}}$ values that are very similar to the Gaussians of the same W_{50} , as do δ functions centered at V_h . We did not test double horn profiles mainly because of the difficulty in modeling them. In addition, generally we do not expect the H α profiles to have as much power at high relative velocities as do double horn profiles for two reasons. First, the horns results from the nearly flat rotation curves of most disk galaxies at large radii, often extending significantly further than the H α distribution (Kennicutt 1989; Martin & Kennicutt 2001). Second, the dip between the horns need not indicate the lack of ISM at systemic velocity but rather may indicate the ISM at the galaxy's center is not primarily neutral.

The filters used in this study are not sufficiently narrow to exclude the [NII] lines at rest $\lambda = 6548.05\text{\AA}$ and 6583.45\AA . Quantum mechanics sets the flux ratio of these two lines to $F_{6548}/F_{6583} = 0.338$. Calling $w_{6583} = F_{\text{[NII]}6583}/F_{\text{H}\alpha}$ then then the fraction of the total line count rate due to H α is

$$\frac{C_{F,\text{H}\alpha}(X)}{C_{F,\text{line}}(X)} = \frac{1}{1 + w_{6583}K_{\text{[NII]}}} \quad (\text{A14})$$

where

$$K_{\text{[NII]}} = \frac{1.0031 \int \lambda G(6583, V_h, W_{50}, \lambda) T_F(\lambda) d\lambda + 0.337 \int \lambda G(6548, V_h, W_{50}, \lambda) T_F(\lambda) d\lambda}{\int \lambda G(6563, V_h, W_{50}, \lambda) T_F(\lambda) d\lambda}. \quad (\text{A15})$$

For a given w_{6583} , then it is a matter of using eq. A15 and A14 to determine the count rate from H α alone, and then using a $f_{\lambda,\text{line}} = G(6563, V_h, W_{50}, \lambda)$ in eq. A12 to get the unit response to H α line emission. We estimate w_{6583} from the R -band absolute magnitude of the line using the empirical relation of Helmboldt et al. (2004) and given in our eq. 5.

NOTES ON INDIVIDUAL HiPASS TARGETS

Here we present notes on individual HiPASS targets. We concentrate on two classes of targets: (1) cases where the measurements were difficult to perform; and (2) ‘‘interesting’’ targets including all those with multiple ELGs, cases where strong outflows are seen, resolved galaxies (near enough to break up into stars), and objects with peculiar or striking morphological features such as rings, or a dominant bulge or nucleus. The sources are listed by their HiPASS/SINGG designation (with NGC, IC, UGC, or ESO designations in parenthesis). In the descriptions we use the following abbreviations: AGN - active galactic nucleus; ELG - emission line galaxy; HSB - high surface brightness;

- LSB - low surface brightness; MSB - moderate surface brightness; DIG - diffuse ionized gas; BCD - blue compact dwarf
 Sy - Seyfert; and the cardinal directions N,S,E,W.
- HIPASS J0005–28** (ESO409-IG015): HSB BCD with a detached HII region located at $r = 61''$ to NW along the optical major axis.
- HIPASS J0019–22**: A possible polar ring (otherwise a faint outer disk ring) of faint HII regions encloses a somewhat off-center elliptical core, featureless in R , but containing a central compact HSB HII complex.
- HIPASS J0039–14A** (NGC 178): This galaxy has a very peculiar morphology, suggestive of a merger. In the R -band, the galaxy is predominantly aligned NS, with two tails extending S. The HSB core is double, with components separated by $9.5''$, with the S component being considerably brighter in $H\alpha$. HII arms to W and E are suggestive of a polar ring, while minor axis fans of extra-planar DIG to north of central components have no obvious power sources. Faint detached HII regions exist to NW of galaxy.
- HIPASS J0135–41** (NGC 625): A well known amorphous / BCD galaxy (Sandage & Brucato 1979; Marlowe et al. 1997). In net $H\alpha$ we see a HSB core, containing a few knots as well as LSB extra-planar features including a nearly complete loop, rising $82''$ from the major axis or the N side. This feature was not seen in the images of Marlowe et al. (1997) but is consistent with the HI kinematics (Cannon et al. 2004).
- HIPASS J0145–43** (ESO245-G005): A resolved LSB IBm/SBm containing bubbly HII regions especially at the bar ends. This galaxy was imaged in HI by Côté, Carignan, & Freeman (2000) while Miller (1996) present NB imaging in $H\alpha$ and [O III].
- HIPASS J0209–10**: There are four ELGs in the field (the most in SR1) - the four bright members of Hickson Compact Group 16. Earlier $H\alpha$ images were presented by Vilchez & Iglesias-Paramo (1998), while spectra were presented by Ribiero et al. (1996) and de Carvalho & Coziol (1999) who found a high incidence of AGN characteristics. All four galaxies have prominent nuclear HSB $H\alpha$, and at least three have a minor axis outflow. S1 (NGC 839) is an inclined disk galaxy with a LINER + Sy2 nuclear spectrum which is prominent in $H\alpha$, while DIG in a minor axis extends out to $r = 31''$. S2 (NGC 838) is a moderately inclined disk with a lumpy nuclear region having a starburst spectrum. Its compact nucleus is surrounded by a HSB $H\alpha$ bright ring with a diffuse wind emanating out the minor axis to $53''$. S3 (NGC 835) and S4 (NGC 833) are closely interacting. S3 is nearly face-on with a double ring morphology ($r \approx 10''$, $43''$) in $H\alpha$ and a LINER + starburst nuclear spectrum. In the R -band a tidal arm extends to the E. S4 is a lopsided moderately inclined barred galaxy. Its nucleus has an Sy2 + LINER spectrum and is embedded to one side of the bar. DIG extends out from the disk at an angle intermediate between major and minor axes, merging with the DIG from S3.
- HIPASS J0216–11C** (NGC 873): A sharp edged HSB spiral well covered in HII regions, somewhat more extended in the R -band than $H\alpha$. Its nucleus is off-center compared to the outer isophotes.
- HIPASS J0221–05**: S1 (NGC 895) is an SBc having a weak $H\alpha$ emitting nucleus, two tight HII region rich arms emerge from the bar with two flocculent armlets between the primary arms. At $r \approx 115''$ the arms merge to form an outer pseudo-ring off-center toward E compared to the nucleus. The displacement may result from interaction with S2 (NGC 895A as assigned by Zaritsky et al. 1993), a very compact nearly circular BCD with LSB $H\alpha$ extensions along its minor axis.
- HIPASS J0224–24**: This collisional ring galaxy system (Lynds & Toomre 1976; Hernquist & Weil 1993) is similar to the Cartwheel galaxy (see e.g. Fosbury & Hawarden 1977; Higdon 1995). The primary S1 (NGC 922) has a “C” shaped morphology and is the ELG with the highest $H\alpha$ luminosity ($L_{H\alpha} = 1.8 \times 10^{42}$ ergs $^{-1}$) in SR1, while we identify the interloper S2 as the compact $H\alpha$ bright galaxy $8.36'$ away to the WNW. Wong et al. (2005b) present a more detailed analysis of this system using a variety of observations including the SINGG SR1 data.
- HIPASS J0256–54** (ESO154-G023): A nearly resolved LSB Sd or Sm whose brightest HII region, (located NE of center) has bipolar bubbles aligned near the minor axis with an overall extent of $64''$.
- HIPASS J0317–22** (ESO481-G017): Face-on spiral with $H\alpha$ concentrated in a parallelogram shaped ring $28''$ in diameter, with a weak sparse HII region distribution beyond.
- HIPASS J0317–41** (NGC 1291): This large face-on SB0 has a distribution of faint HII regions that traces tightly wound arms or pseudo ring at $r = 4.7'$. A swirling pattern of DIG, dominates the central $H\alpha$ morphology. This structure is devoid of HII regions and increases in surface brightness toward the nuclear region, reminiscent of the DIG in the bulge of M31 (Ciardullo et al. 1988). The measurements of this galaxy are difficult because the nucleus is saturated in the R -band (hence the nucleus is masked from our image) and the galaxy’s sparse population of HII regions extends to the edge of the frame or beyond.
- HIPASS J0320–52** (NGC 1311): Edge-on Sd or Sm with HII knots along the major axis and DIG streamers along the minor axis.
- HIPASS J0342–13**: This system is dominated by S1 (NGC 1421), a highly inclined SBb galaxy whose brightest two arms, bar and nucleus are well covered with HSB HII regions. Its dwarf companion S2 could easily be mistaken for a background galaxy, except for its two HSB nuclear HII regions.
- HIPASS J0355–42** (NGC 1487): A well known merger (Vorontsov-Velyaminov 1959). Our R image shows two nuclei separated by $10.3''$ on a nearly NS line, with a third similar hotspot (or nucleus) located $26''$ to the E of the northern, while two long tidal tails stretch out to $\sim 75''$. The $H\alpha$ image is dominated by the HSB core surrounding the three hotspots, while fainter HII regions can be seen all along the tidal arms.
- HIPASS J0359–45**: S1 (The Horologium Dwarf) is a face-on LSB dwarf with sparse population of dozens of faint HII regions. S2 (ESO249-G035) is an edge-on LSB to MSB disk galaxy.

HIPASS J0403–01: A very difficult galaxy to measure due to the supposition of a bright (saturated) star and pervading Galactic cirrus emission in $H\alpha$. This galaxy is discussed in Sec. 3.10 while Fig. 6a shows an expanded image of the galaxy.

HIPASS J0403–43: This is the well known starburst pair NGC 1512/NGC 1510 (S1/S2), strongly interacting galaxies sharing a common HI envelope (Hawarden, et al. 1979). S1 is a large SBb with a central starburst ring surrounding its nucleus and embedded in a bar that is otherwise devoid of $H\alpha$. An outer ring, well populated with HII regions, circles the bar, while a weak distribution of HII regions extends to the edges of the frame. S2 is an amorphous/BCD galaxy that dominates over S1 in total $H\alpha$ flux. Its $H\alpha$ morphology is strongly concentrated toward two central knots, separated by $4''$, with radial filaments including an apparent jet toward the SW.

HIPASS J0409–56 (NGC 1533): This is an HSB face-on SB0, having bar length of $40''$ with a few faint HII regions over the optical face, as well as the more distant ELDots discussed by Ryan-Weber et al. (2004). This is the second difficult to measure galaxy discussed in Sec. 3.10 and displayed in Fig. 6b.

HIPASS J0430–01 (UGC3070): Sm galaxy with parallelogram outer ring having dimensions $36'' \times 64''$ enclosing a central bar.

HIPASS J0441–02 (NGC 1637): Three armed asymmetric spiral having a sharp change in the HII regions properties. Interior to $r \approx 1.5'$ there is a modest density of bright HII regions, exterior to this there is a sparse distribution of faint HII regions out to $r \sim 3.6'$.

HIPASS J0454–53 (NGC 1705): An amorphous / BCD galaxy well known for its off-center super star cluster and strong galactic wind. Our $H\alpha$ image shows minor axis arcs, not seen by Meurer et al. (1992), which reach out to $90''$ to the S, and $94''$ to the NNW.

HIPASS J0456–42 (ESO252-IG001): Sm/Im galaxy superimposed on an edge-on background galaxy. Contains a curious near linear $H\alpha$ arc through center along minor axis.

HIPASS J0503–63: S1 (ESO085–G034) is an inclined Sa with faint tightly wound spiral arms more apparent in $H\alpha$. Its HII distribution is brighter on the E side toward S2, its compact dwarf companion, which has two bright HII regions, and has not been previously cataloged (according to NED).

HIPASS J0504–16: This system contains two LSB galaxies. S1 is a large face-on SBcd with HII regions over its face and two long outer arms. The longest stretches SW toward S2, a small LSB galaxy, not previously cataloged (according to NED), with a few faint HII regions on its SE side.

HIPASS J0506–31 (NGC 1800): Another well studied amorphous / BCD with extra-planar $H\alpha$ and a HSB core region (e.g. Hunter et al. 1994; Marlowe et al. 1997). Most of the star formation and extra-planar $H\alpha$ is located in the E half of the galaxy.

HIPASS J0507–37 (NGC 1808): A well studied starburst with an embedded Sy2 nucleus (Veron-Cetty & Veron 1985). The starburst corresponds to the lumpy core $\sim 22''$ across with intense $H\alpha$ emission, embedded in an oval shaped bar $270''$ long. HII regions trace a somewhat smaller and tighter integral symbol shaped bar $192''$ long. Spiral arms emerge from the larger bar to form a nearly complete figure-eight pseudo-ring containing a few faint HII regions. There are numerous dust lanes in the central region, and an edge-darkened spray of diffuse dust obscuration emanating from the core toward the NE projecting out to at least $40''$, previously noted by Garrison & Walborn (1974) (cf. Veron-Cetty & Veron 1985), is indicative of an edge-darkened dust entrained outflow.

HIPASS J0514–61: There are three ELGs in this system. S1 (ESO119-G048) is an SBa, which has a $143''$ long oval bar resembling a strongly nucleated HSB elliptical galaxy. Two weak arms start at the bar's ends to form a faint pseudo-ring. Sparsely distributed HII regions populate the region from the bar minor-axis to the faint outer arms. S2 (ESO119-G044) is a face-on Sbc having a fairly random distribution of HII regions covers its optical face. S3 is a compact HSB SBab with strong line emission along the bar and much of the tight spiral arms that emerge from it.

HIPASS J1054–18: S1 (ESO569-G020) is a moderate to LSB spiral containing a small bar, invisible in $H\alpha$, and flocculent HII region rich arms. S2 (ESO569-G021) is a small disk galaxy with a compact nucleus, and an HSB $H\alpha$ ring ($12''$ diameter).

HIPASS J1105–00 (NGC 3521): This moderately inclined bulge dominated Sb galaxy has a HSB nucleus that is saturated in R , and masked out in our net $H\alpha$ image. Hence our $F_{H\alpha}$ and $S_e(H\alpha)$ measurements are underestimated. However examination of the NB images suggests that nucleus does not significantly contribute to the total $F_{H\alpha}$. There is an apparent $H\alpha$ ring at $r \approx 25''$, while the disk beyond that to $r = 116''$ is well covered by HII regions and DIG.

HIPASS J1109–23 (IC 2627): This is a face-on grand-design Sc galaxy that is somewhat lopsided on large scales. At its heart is a very compact HSB ring of HII emission at $r = 1.8''$ surrounding the nucleus. The two arms are well delineated in bright HII regions.

HIPASS J1131–02: S1 (UGC06510) is a face-on SBc with flocculent $H\alpha$ rich arms and a small $16''$ long bar containing a strong nucleus in R . S2 is an edge on disk with strong line emission along much of its length. S3 is a small source, not previously cataloged (according to NED), located between S1 and S2 that is similar to an ELDot except that it is clearly two faint connected line emitting knots separated by $3.5''$.

HIPASS J1303–17c (UGCA320,DDO161): This is a partly resolved, edge-on low surface brightness disk, with nearly rectangular bulge or bar $1'$ across containing numerous clusters or knots and a well defined nucleus. HII regions at the edge of the bulge have DIG extending out the minor axis especially on the N side. This source was imaged in HI by Côté, Carignan, & Freeman (2000).

HIPASS J1337–29 (NGC 5236): The well studied Messier 83 is a large face-on SBb. The thick bar is $199''$ long and contains numerous dust lanes. The bar dust lanes terminate in a central, knotty very HSB region (in both R -band and $H\alpha$) $14''$ across - the central starburst. Numerous bright HII regions have a high covering factor, especially along

the two arms, out to $R \sim 290''$. There the $H\alpha$ distribution is largely truncated, as pointed out by Kennicutt (1989) and Martin & Kennicutt (2001), while the UV light profile shows no truncation (Thilker et al. 2005). However, a few fainter HII regions can be seen out to the edge of our frame.

HIPASS J1339–31A (NGC 5253): Like the other amorphous / BCD galaxies, we see smooth elliptical outer isophotes and a knotty core which has been imaged extensively by HST (e.g. Calzetti et al. 1997). This source has the most extreme star formation properties, in terms of Σ_{SFR} and EW_{50} of any of the SR1 galaxies. At large radii the $H\alpha$ morphology is bubbly along the minor axis. A well known dust lane darkens the SE minor axis.

HIPASS J2149–60: A spectacular system consisting of a binary spiral pair with a compact dwarf in between. S1 (NGC 7125) is a moderately inclined Sb with an $H\alpha$ bright inner ring, a nucleus devoid of $H\alpha$ and thin MSB outer arms. S2 (NGC 7126) is a low inclination SBbc with a small $H\alpha$ bright bar, two main arms and many armlets all rich in HII regions. S3, located between them is a small almost featureless LSB galaxy containing one HII region and some DIG. All three sources correspond to HI detections in the VLA map of Nordgren et al. (1997). A fourth HI source identified by them (their 145G17B) is not apparent in $H\alpha$.

HIPASS J2202–20: S1 (NGC 7184) is a dusty inclined SBbc with an inner ring enclosing a foreshortened bar which contains a compact $H\alpha$ bright nucleus. Two symmetric arms, well traced by HII regions emerge from the bar, become flocculent in their HII distribution, and regain distinction at the outermost radii. S2 is a small featureless edge-on disk with MSB line emission along its length.

HIPASS J2334–36 (IC 5332): This is a large angular extent face-on Sc galaxies with two arm morphology in R all the way to the compact bulge, but a flocculent distribution of bubbly HII regions.

HIPASS J2343–31 (UGCA442): A partly-resolved edge-on LSB galaxy showing several HII regions along the major axis having loop morphologies. This galaxy was imaged in HI by Côté, Carignan, & Freeman (2000) and HST WFPC2 by Karachentsev et al. (2003) and Mould (2005).

HIPASS J2352–52 (ESO149-G003): This is an edge-on LSB to MSB disk, flared at large radii, having minor axis $H\alpha$ filaments emanating from the central region despite the lack of a central HSB core.

REFERENCES

- Alard, C. 2000, *A&AS*, 144, 363
 Barnes, D.G., et al. 2001, *MNRAS*, 322, 486
 Bertin, E. & Arnouts, S. 1996, *A&AS*, 117, 393
 Blanton, M.R., Lin, H., Lupton, R.H., Miller Maley, F., Young, N., Zehavi, I., & Loveday, J. 2003, *AJ*, 125, 2276
 Blanton, M.R., et al. 2003, *ApJ*, 592, 819
 Blanton, M.R., Lupton, R.H., Schlegel, D.J., Strauss, M.A., Brinkmann, J., Fukugita, M., & Loveday, J., 2005, *ApJ*, submitted
 Bothun, G., Impey, C., & McGaugh, S., 1997, *PASP*, 109, 745
 Brinchmann, J., Charlot, S., White, S.D.M., Tremonti, C., Kauffmann, G., Heckman, T., & Brinkmann, J. 2004, *MNRAS*, 351, 1151 (B04)
 Bushouse, H. & Simon, B. 1998, "Synphot User's Guide", Baltimore: STSci.
 Calzetti, D., Kinney, A.L., & Storchi-Bergmann, T. 1994 *ApJ*, 429, 582
 Calzetti, D., Meurer, G.R., Bohlin, R.C., Garnett, D.R., Kinney, A.L., Leitherer, C., & Storchi-Bergmann, T. 1997, *AJ*, 114, 1834
 Calzetti, D., Armus, L., Bohlin, R.C., Kinney, A.L., Korneef, J., & Storchi-Bergmann, T. 2000, *ApJ*, 533, 682
 Cannon, J.M., McClure-Griffiths, N.N., Skillman, E.D., & Côté, S. 2004, *ApJ*, 607, 274
 Cardelli, J.A., Clayton, G.C., & Mathis, J.S. 1989, *ApJ*, 345, 245
 Ciardullo, R., Rubin, V.C., Jacoby, G.H., Ford, H.C., & Ford, W.K. 1988, *AJ*, 95, 438
 Colless, M., et al. 2001, *MNRAS*, 328, 1039
 Côté, S., Carignan, C., & Freeman, K.C. 2000, *AJ*, 120, 3027
 Dalcanton, J.J., Spergel, D.N., Gunn, J.E., Smith, M., & Schneider, D.P. 1997, *AJ*, 114, 635
 de Carvalho, R.R., & Coziol, R. 1999, *AJ*, 117, 1657
 de Vaucouleurs, G., de Vaucouleurs, A., Corwin, H.G., Buta, R.J., Paturel, G., & Fouqué, P. 1991, *Third Reference Catalog of Bright Galaxies*, (Springer-Verlag, New York)
 Disney, M.J. 1976, *Nature*, 263, 573
 Doyle, M.T. et al., 2005, *MNRAS*, 361, 34
 Drinkwater, M.J., Gregg, M.D., Hilker, M., Bekki, K., Couch, W.J., Ferguson, H.C., Jones, J.B., & Phillips, S.S. 2003, *Nature*, 423, 519
 Fanelli, M.N., O'Connell, R.W., & Thuan, T.X. 1988, *ApJ*, 334, 665
 Ferguson, A.M.N., Wyse, R.F.G., Gallagher, III, J.S., & Hunter, D.A. 1996, *AJ*, 111, 2265
 Ferguson, A.M.N., Wyse, R.F.G., Gallagher, III, J.S., & Hunter, D.A. 1998, *ApJ*, 506, L19
 Fosbury, R.A.E., & Hawarden, T.G. 1977, *MNRAS*, 178, 473
 Fukugita, M., Ichikawa, T., Gunn, J.E., Doi, M., Shimasaku, M., & Schneider, D.P. 1996, *AJ*, 111, 1748
 Gallego, J., Zamorano, J., Aragón-Salamanca, A., & Rego, M. 1995, *ApJ*, 455, L1
 Gallego, J., Zamorano, J., Rego, M., Alonso, O., & Vitoras, A.G. 1996, *A&AS*, 120, 323
 Garrison, R.F., & Walborn, N.R. 1974, *JRASC*, 68, 117
 Gerola, H., Seiden, P.E., & Schulman, L.S. 1980, *ApJ*, 242, 517
 Gil de Paz, A., Madore, B.F., & Pevunova, O. 2003, *ApJS*, 147, 29
 Glazebrook, K., Baldry, I., Blanton, M.R., Brinkmann, J., Connolly, A., Csabai, I., Fukugita, M., Ivezić, Z., Loveday, J., Meiksen, A., Nichol, R., Peng, E., Schneider, D.P., SubbaRao, M., Tremonti, C., & York, D.G. 2003, *ApJ*, 587, 55
 Gronwall, C., Salzer, J.J., Sarajedini, V.L., Jangren, A., Chomiuk, L., Moody, J.W., Frattare, L.M., & Boroson, T.A. 2004, *AJ*, 127, 1943
 Hamuy, M., Walker, A.R., Suntzeff, N.B., Gigoux, P., Heathcote, S.R., & Phillips, M.M. 1992, *PASP*, 104, 533
 Hamuy, M., Walker, A.R., Suntzeff, N.B., Gigoux, P., Heathcote, S.R., & Phillips, M.M. 1994, *PASP*, 106, 566
 Hanish, D.J., et al. 2006, *ApJ*, submitted
 Hawarden, T.G., van Woerden, H., Mebold, U., Goss, W.M., & Peterson, B.A. 1979, *A&A*, 76, 230
 Heckman, T.M. 2005, in "Starbursts: From 30 Doradus to Lyman Break Galaxies", eds. R. de Grijs and R.M. González Delgado, *Astrophysics & Space Science Library*, Vol. 329. (Dordrecht: Springer), p. 3
 Helou, G., Khan, I.R., Malek, L., & Boehmer, L. 1988, *ApJS*, 68, 151
 Hernquist, L., & Weil, M.L. 1993, *MNRAS*, 261, 804
 Helmboldt, J.F., Walterbos, R.A.M., Bothun, G.D., O'Neil, K., & de Blok, W.J.G. 2004, *ApJ*, 613, 914
 Higdon, J.L. 1995, *ApJ*, 455, 524
 Hoopes, C.G., Walterbos, R.A.M., & Bothun, G.D. 2001, *ApJ*, 559, 878
 Hopkins, A.M. 2004, *ApJ*, 615, 209
 Hunter, D.A., Hawley, W.N., & Gallagher, III, J.S. 1993, *AJ*, 106, 1797
 Hunter, D.A., van Woerden, H., & Gallagher, III, J.S. 1994, *ApJS*, 91, 79
 Hunter, D.A., & Elmegreen, B.G. 2004, *AJ*, 128, 2170
 James, P.A., Shane, N.S., Beckmann, J.E., Cardwell, A., Collins, C.A., Etherton, J., de Jong, J.S., Fathi, K., Knapen, J.H., Peletier, R.F., Percival, S.M., Pollacco, D.L., Seigar, M.S., Stedman, S., & Steele, I.A. 2004, *A&A*, 414, 23
 Jansen, R.A. 2000, Ph.D. thesis, Kapteyn Astronomical Institute, Univ. Groningen
 Jansen, R.A., Fabricant, D., Franx, M., Caldwell, N. 2000, *ApJS*, 126, 331
 Karachentsev, I.D., Grebel, E.K., Sharina, M.E., Dolphin, A.E., Geisler, D., Guhathakurta, P., Hodge, P.W., Karachentseva, V.E., Sarajedini, A., & Seitzer, P. 2003, *A&A*, 404, 93
 Karachentsev, I.D., Karachentseva, V.E., Huchtmeier, W.K., & Markov, D.I., 2004, *AJ*, 127, 2031.

- Kauffmann, G., Heckman, T.M., White, S.D.M., Charlot, S., Tremonti, C., Brinchmann, J., Bruzual, G., Peng, E.W., Seibert, M., Bernardi, M., Blanton, M., Brinkmann, J., Castander, F., Csabai, I., Fukugita, M., Ivezić, Z., Munn, J.A., Nichol, R.C., Padmanabhan, N., Thakar, A.R., Weinberg, D.H., & York, D. 2003, *MNRAS*, 341, 33
- Kennicutt, R.C. 1983, *ApJ*, 272, 54
- Kennicutt, R.C. 1989, *ApJ*, 344, 685
- Kennicutt, R.C. 1998, *ApJ*, 498, 541
- Kennicutt, R.C., Tamblyn, P., & Congdon, C.E. 1994, *ApJ*, 435, 22
- Kilborn, V.A. et al., 2002, *AJ*, 124, 690
- Kniazev, A.Y., Grebel, E.K., Pustilnik, S.A., Pramskij, A.G., Kniazeva, T.F., Prada, F., & Harbeck, D. 2004, *AJ*, 127, 704
- Kodama, T., Balogh, M.L., Smail, I., Bower, R.G., & Nakata, F. 2004, *MNRAS*, 354, 1103
- Koribalski et al. 2004, *AJ*, 128, 16
- Kroupa, P. 2001, *MNRAS*, 322, 231
- Lee, J.C., Salzer, J.J., Impey, C., Thuan, T.X., Gronwall, C. 2002, *AJ*, 124, 3088
- Leitherer, C. et al., 1999, *ApJS*, 123, 3
- Lejeune, T., Cuisinier, F., & Buser, R. 1997, *A&AS*, 125, 229
- Lynden-Bell, D., Faber, S.M., Burstein, D., Davies, R.L., Dressler, A., Terlevich, R.J., & Wegner, G. 1988 *ApJ*, 326, 19
- Lynds, R. & Toomre, A. 1976, *ApJ*, 209, 382
- Maddox, S.J., Sutherland, W.J., Efstathiou, G., & Loveday, J. 1990, *MNRAS*, 243, 692
- Macció, A.V., Governato, F., & Horrelou C. 2005, *MNRAS*, 359, 941
- Marlowe, A.T., Meurer, G.R., Heckman, T.M., & Schommer, R. 1997, *ApJS*, 112, 285
- Martin, C.L. 1998, *ApJ*, 506, 222
- Martin, C.L., & Kennicutt, R.C. 2001, *ApJ*, 555, 301
- Martins, F., Schaerer, D., & Hillier, D.J. 2005, *A&A*, in press (astro-ph/0503346)
- Massey, P., Strobel, K., Barnes, J.V., Anderson, E. 1988, *ApJ*, 328, 315
- McCall, M.L., Rybski, P.M., & Shields, G.A. 1985, *ApJS*, 57, 1
- McCaugh, S.S., Schombert, J.M., Bothun, G.D., & de Blok, W.J.G. 2000, *ApJ*, 533, L99
- Meurer, G.R., Freeman, K.C., Dopita, M.A., & Cacciari, C. 1992, *AJ*, 103, 60
- G.R. Meurer, T.M. Heckman, & D. Calzetti, 1999 *ApJ*, 521, 64
- Meurer, G.R., & Seibert, M. 2001 in "Starburst Galaxies: Near and Far", eds., L. Tacconi, D. Lutz (Berlin: Springer), p. 272-277
- Meyer, M.J., et al. 2004, *MNRAS*, 350, 1195
- Miller, B.W. 1996, *AJ*, 112, 991
- Monet, D., Bird A., Canzian, B., Dahn, C., Guetter, H., Harris, H., Henden, A., Levine, S., Luginbuhl, C., Monet, A. K. B., Rhodes, A., Rieke, B., Sell, S., Stone, R., Vrba, F., & Walker, R. 1998, The USNO-A2.0 Catalogue, (U.S. Naval Observatory, Washington DC)
- Moshir, M., Kopan, M., Conrow, G., McCallon, T., Hacking, H., Gregorich, P., Rohrbach, D., Melnyk, G., Rice, M., Fullmer, W., et al. 1990, Infrared Astronomical Satellite Catalogs, The Faint Source Catalog, Version 2.0
- Mould, J.R., et al. 2000, *ApJ*, 529, 786
- Mould, J. 2005, *AJ*, 129, 698
- Moustakas, J. & Kennicutt, R.C., Jr. 2006, *ApJS*, in press, (astro-ph/0511729)
- Nordgren, T.E., Chengalur, J.N., Salpeter, E.E., Terzian, Y. *AJ*, 114, 913
- Oke, J.B. 1990, *AJ*, 99, 1621
- Putman, M.E., et al. 2002, *AJ*, 123, 873
- Pérez-González, P.G., Zamorano, J., Gallego, J., Aragón-Salamanca, & Gil de Paz, A. 2003, *ApJ*, 591, 827
- Pérez-González, P.G., Rieke, G.H., Egami, E., Alonso-Herrero, A., Dole, H., Papovich, C., Blaylock, M., Jones, J., Rieke, M., Rigby, J., Barmby, P., Fazio, G.G., Huang, J., & Martin, C. 2005, *ApJ*, 630, 82
- Ribiero, A.L.B., de Carvalho, R.R., Coziol, R., Capelato, H.V., & Zepf, S. *ApJ*, 463, L5.
- Rice, W., Lonsdale, C.J., Soifer, B.T., Neugebauer, G., Kopan, E.L., Lloyd, L.A., de Jong, T., & Habing, H.J. 1988, *ApJS*, 68, 91
- Roberts, M.S. 1962, *AJ*, 67, 437
- Ryan-Weber, E. et al., 2002, *AJ*, 124, 1954
- Ryan-Weber, E. et al. 2004, *AJ*, 127, 1431
- Ryder, S.D., & Dopita, M.A. 1994, *ApJ*, 430, 142
- Salzer, J.J., Gronwall, C., Lipovetsky, V.A., Kniazev, A., Moody, J.W., Boroson, T.A., Thuan, T.X., Izotov, Y.I., Herrero, J.L., Frattare, L.M. 2000, *AJ*, 120, 80
- Sandage, A. & Brucato, R. 1979, *AJ*, 84, 472
- Sanders, D.B., & Mirabel, I.F. 1996, *ARAA*, 34, 749
- Schlegel, D.J., Finkbeiner, D.P., & Davis, M. 1998, *ApJ*, 500, 525
- Salpeter, E.E. 1955, *ApJ*, 121, 161
- Schmidt, B.P. et al. 1998, *ApJ*, 507, 46
- Smith, L.J., Norris, R.P.F., & Crowther, P.A. 2002, *MNRAS*, 337, 1309
- Smith, R.C., & the MCELS Team 1998, *PASA*, 15, 163
- Staveley-Smith, L., Wilson, W.E., Bird, T.S., Disney, M.J., Ekers, R.D., Freeman, K.C., Haynes, R.F., Sinclair, M.W., Vaile, R.A., Webster, R.L. & Wright, A.E. 1996, *PASA*, 13, 243
- Strauss, M.A., et al., 2002, *AJ*, 124, 1810
- Strauss, M.A., Cen, R., & Ostriker, J.P. 1993, *ApJ*, 408, 389
- Taylor, E.N., & Webster, R.L. 2005, *ApJ*, submitted (astro-ph/0501514)
- Thilker, D.A. et al. 2005, *ApJ*, 619, L79.
- Tonry, J.L., Blakeslee, J.P., Ajhar, E.A., Dressler, A. 1998, *ApJ*, 530, 625
- Tremonti, C.A., Heckman, T.M., Kauffmann, G., Brinchmann, J., Charlot, S., White, S.D.M., Seibert, M., Peng, E.W., Schlegel, D.J., Uomoto, A., Fukugita, M., & Brinkmann, J. 2004, *ApJ*, 613, 898
- Treyer, M.A., Ellis, R.S., Milliard, B., Donas, J. & Bridges, T.J. 1998, *MNRAS*, 300, 303
- Veron-Cetty, M.-P., & Veron, P. 1985, *A&A*, 145, 425
- Vilchez, J.M., & Iglesias-Paramo, J. *ApJS*, 117, 1.
- Vorontsov-Velyaminov, B.A. 1959, "Atlas and Catalog of Interacting Galaxies", Sternberg Institute, Moscow: Moscow State University
- Wegner, G., Salzer, J.J., Jangren, A., Gronwall, C., & Melbourne, J. 2003, *AJ*, 125, 2373
- Willick, J.A., Strauss, M.A., Dekel, A. & Kolatt, T. 1997, *ApJ*, 486, 629
- Willick, J.A. & Strauss, M.A. 1998, *ApJ*, 507, 64
- Wong, I., et al. 2005a, *MNRAS*, submitted
- Wong, I., et al. 2005b, *MNRAS*, in press, (astro-ph/0605613)
- York, D.G., et al. 2000, *AJ*, 120, 1579
- Young, J.S., Allen, L., Kenney, J.D.P., Lesser, A. & Rownd, B. 1996, *AJ*, 112, 1903
- Zaritsky, D., Smith, R., Frenk, C., and White, S.D.M. 1993, *ApJ*, 405, 464
- Zwaan, M.A., Briggs, F.H., Sprayberry, D., & Sorar, E. 1997, *ApJ*, 490, 173
- Zwaan, M.A., et al. 2004, *MNRAS*, 350, 1210

TABLE 6
SOURCE IDENTIFICATION AND MEASUREMENT APERTURES FOR SR1

HIPASS+ (1)	Optical ID (2)	Morph (3)	RA (4)	Dec (5)	Filters (6)	r_{\max} (7)	a/b (8)	θ (9)
J0005-28	ESO409-IG015		00 05 31.7	-28 05 53	6568/28;R	65	1.72	141
J0019-22	MCG-04-02-003	.I..9*P	00 19 11.5	-22 40 06	6568/28;R	75	1.60	3
J0031-22	ESO473-G024	.IBS9..	00 31 22.2	-22 46 02	6568/28;R	72	1.41	26
J0039-14a	NGC178	.SBS9..	00 39 08.2	-14 10 29	6605/32;R	139	2.12	9
J0043-22	IC1574	.IBS9..	00 42 27.0	-22 06 19	6568/28;R	71	1.73	172
J0135-41	NGC625	.SBS9\$/	01 35 06.2	-41 26 04	6568/28;R	238	2.37	94

NOTE. — *Sample portion of table.*

TABLE 7
INTRINSIC QUANTITIES FOR SR1

Designation (1)	M_R (2)	$r_e(R)$ (3)	$r_{90}(R)$ (4)	$\mu_{e,0}(R)$ (5)	$\log(F_{H\alpha})$ (6)	$r_e(H\alpha)$ (7)	$r_{90}(H\alpha)$ (8)	$\log(\text{SFR})$ (9)	$\log(\text{SFA})$ (10)	$EW_{50,0}$ (11)
J0005–28	-15.51 ± 0.03	0.773 ± 0.013	2.115 ± 0.054	22.33 ± 0.03	-12.32 ± 0.02	0.453 ± 0.002	0.860 ± 0.026	-2.24	-1.55 ± 0.02	292.8 ± 3.2
J0019–22	$-15.50 \pm 0.03^\dagger$	0.912 ± 0.016	2.934 ± 0.023	22.70 ± 0.03	$-13.14 \pm 0.08^\ddagger$	0.595 ± 0.191	–	-3.13	-2.68 ± 0.18	27.9 ± 3.4
J0031–22	-14.06 ± 0.06	0.909 ± 0.029	2.035 ± 0.088	24.17 ± 0.03	-13.08 ± 0.04	0.682 ± 0.019	1.868 ± 0.159	-3.29	-2.95 ± 0.03	78.7 ± 4.3
J0039–14a	$-19.01 \pm 0.02^\dagger$	2.304 ± 0.013	6.038 ± 0.218	21.00 ± 0.02	$-12.06 \pm 0.03^\dagger$	2.141 ± 0.011	5.159 ± 0.167	-1.24	-1.90 ± 0.03	56.8 ± 3.4
J0043–22	-14.47 ± 0.03	0.738 ± 0.005	1.333 ± 0.008	23.30 ± 0.02	-13.34 ± 0.20	0.622 ± 0.082	1.257 ± 0.121	-3.96	-3.55 ± 0.11	9.5 ± 3.6
J0135–41	-17.30 ± 0.02	1.309 ± 0.012	3.109 ± 0.053	21.61 ± 0.02	-11.33 ± 0.07	0.436 ± 0.021	1.404 ± 0.525	-2.02	-1.30 ± 0.03	222.9 ± 7.3
J0145–43	-16.14 ± 0.09	1.869 ± 0.075	3.554 ± 0.175	23.60 ± 0.02	-11.93 ± 0.05	2.181 ± 0.049	3.244 ± 0.234	-2.59	-3.27 ± 0.05	30.6 ± 4.4
J0156–68	-16.23 ± 0.03	1.589 ± 0.020	3.384 ± 0.061	23.13 ± 0.02	-13.32 ± 0.05	1.515 ± 0.031	2.413 ± 0.205	-2.71	-3.07 ± 0.05	27.3 ± 2.9
J0209–10:S1	$-20.98 \pm 0.02^\dagger$	3.338 ± 0.030	10.708 ± 0.254	19.59 ± 0.02	$-12.46 \pm 0.08^\dagger$	1.488 ± 0.191	7.446 ± 1.519	-0.62	-0.97 ± 0.04	83.4 ± 4.9
J0209–10:S2	-21.16 ± 0.02	2.348 ± 0.013	8.627 ± 0.118	18.62 ± 0.02	-11.83 ± 0.02	1.500 ± 0.026	4.527 ± 0.264	0.04	-0.32 ± 0.01	183.0 ± 4.9
J0209–10:S3	-21.88 ± 0.02	4.829 ± 0.050	19.870 ± 0.290	19.34 ± 0.03	-12.12 ± 0.08	3.239 ± 0.148	17.297 ± 2.324	-0.16	-1.18 ± 0.04	39.9 ± 5.2
J0209–10:S4	-21.22 ± 0.02	3.574 ± 0.007	8.476 ± 0.033	19.46 ± 0.02	-12.88 ± 0.25	2.990 ± 0.241	7.640 ± 1.399	-1.01	-1.96 ± 0.19	11.1 ± 4.9

NOTE. — *Sample portion of table.*

TABLE 8
CORRECTIONS USED IN FLUX MEASUREMENTS

HIPASS+ (1)	$A_{H\alpha,G}$ (2)	M'_R (3)	$A_{H\alpha,i}$ (4)	$A_{R,i}$ (5)	w_{6583} (6)	$k_{[NII]}$ (7)
J0005–28	0.04	-15.51	0.24	0.12	0.052	0.352
J0019–22	0.05	-15.50	0.24	0.12	0.052	0.353
J0031–22	0.05	-14.06	0.16	0.08	0.034	0.381
J0039–14a	0.05	-19.01	0.64	0.32	0.148	0.797
J0043–22	0.04	-14.47	0.18	0.09	0.038	0.525
J0135–41	0.04	-17.30	0.40	0.20	0.089	0.488
J0145–43	0.04	-16.14	0.29	0.14	0.063	0.492
J0156–68	0.07	-16.23	0.30	0.15	0.065	0.893
J0209–10:S1	0.06	-20.98	1.10	0.55	0.267	1.335
J0209–10:S2	0.06	-21.16	1.16	0.58	0.283	1.335
J0209–10:S3	0.06	-21.88	1.41	0.71	0.351	1.335
J0209–10:S4	0.06	-21.22	1.18	0.59	0.288	1.335

NOTE. — *Sample portion of table.*

TABLE 9
MEDIAN IMAGE QUALITY STATISTICS

Image type	Seeing	Limiting mag or flux	Limiting surface brightness	Limiting EW
R or continuum	$1.57''$	22.73 ABmag	$26.95 \text{ ABmag arcsec}^{-2}$...
NB	$1.56''$	20.83 ABmag	$25.76 \text{ ABmag arcsec}^{-2}$...
Net $H\alpha$	$1.61''$	$2.6 \times 10^{-16} \text{ erg cm}^{-2} \text{ s}^{-1}$	$2.9 \times 10^{-18} \text{ erg cm}^{-2} \text{ s}^{-1} \text{ arcsec}^{-2}$	3.3\AA